DIPG harbour alterations targetable by MEK inhibitors, with acquired resistance mechanisms overcome by combinatorial inhibition

Elisa Izquierdo[1], Diana M Carvalho[1], Alan Mackay[1], Sara Temelso[1], Jessica KR Boult[2], Giulia Pericoli[3], Elisabet Fernandez[1], Molina Das[1], Valeria Molinari[1], Yura Grabovska[1], Rebecca F Rogers[1], Maria Antonietta Ajmone-Cat[4], Paula Z Proszek[5], Mark Stubbs[6], Sarita Depani[7], Patricia O'Hare[7], Lu Yu[8], Georgia Roumelioti[8], Jyoti S Choudhary[8], Matthew Clarke[1], Amy R Fairchild[9], Thomas S Jacques[9], Richard G Grundy[10], Lisa Howell[11], Susan Picton[12], Jenny Adamski[13], Shaun Wilson[14], Juliet C Gray[15], Bassel Zebian[16], Lynley V Marshall[17,18], Fernando Carceller[17,18], Jacques Grill[19], Maria Vinci[3], Simon P Robinson[2], Michael Hubank[5], Darren Hargrave[7,9] and Chris Jones[1]

[1]Division of Molecular Pathology, Institute of Cancer Research, London, UK; [2]Division of Radiotherapy and Imaging, The Institute of Cancer Research, London, UK; [3]Department of Haematology/Oncology, Gene and Cell Therapy, Bambino Gesù Children's Hospital-IRCCS, Rome, Italy; [4]National Centre for Drug Research and Evaluation, Istituto Superiore di Sanità, Rome, Italy; [5]Molecular Diagnostics, Royal Marsden Hospital NHS Trust, Sutton, UK; [6]Division of Cancer Therapeutics, Institute of Cancer Research, London, UK; [7]Department of Haematology and Oncology, Great Ormond Street Hospital for Children NHS Foundation Trust, London, UK; [8]Division of Cancer Biology, Institute of Cancer Research, London, UK; [9]UCL Great Ormond Street Institute for Child Health, London; [10]Children's Brain Tumour Research Centre, School of Medicine, University of Nottingham, UK; [11]Alder Hey Children's NHS Foundation Trust, Liverpool, UK; [12]Leeds Children's Hospital, Leeds, UK; [13]Birmingham Women's and Children's Hospital, Birmingham, UK; [14]Oxford University Hospitals NHS Foundation Trust, Oxford, UK; [15]Centre for Cancer Immunology, University of Southampton, UK; [16]Department of Neurosurgery, Kings College Hospital NHS Trust, London, UK; [17]Division of Clinical Studies, The Institute of Cancer Research, London, UK; [18]Children & Young People's Unit, Royal Marsden Hospital NHS Trust, Sutton, UK; [19]Department of Pediatric and Adolescent Oncology and INSERM Unit U891, Team "Genomics and Oncogenesis of Pediatric Brain Tumors", Gustave Roussy and University Paris-Saclay, Villejuif, France

1

Lead contact and correspondence to:

Chris Jones, Division of Molecular Pathology, The Institute of Cancer Research, 15 Cotswold

Road, Sutton, Surrey, SM2 5NG, UK, chris.jones@icr.ac.uk, +44 (0)20 8722 4416

Running title: MEK inhibition and resistance in DIPG

Conflict of interest statement:

The authors declare no conflicts of interest pertaining to this manuscript.

2

ABSTRACT

The survival of children with DIPG remains dismal, with new treatments desperately needed. In a prospective biopsy-stratified clinical trial, we combined detailed molecular profiling and drug screening in newly-established patient-derived models *in vitro* and *in vivo*. We identified *in vitro* sensitivity to MEK inhibitors in DIPGs harbouring MAPK pathway alterations, however treatment of PDX models and a patient at relapse failed to elicit a significant response. We generated trametinib-resistant clones in a *BRAF*_G469V model through continuous drug exposure, and identified acquired mutations in *MEK1/2* with sustained pathway up-regulation. These cells showed hallmarks of mesenchymal transition, and expression signatures overlapping with inherently trametinib-insensitive patient-derived cells, predicting sensitivity to dasatinib. Combined trametinib and dasatinib showed highly synergistic effects *in vitro* and on *ex vivo* brain slices. We highlight the MAPK pathway as a therapeutic target in DIPG, and show the importance of parallel resistance modelling and combinatorial treatments for meaningful clinical translation.

STATEMENT OF SIGNIFICANCE

We report alterations in the MAPK pathway in DIPGs to confer initial sensitivity to targeted MEK inhibition. We further identify for the first time the mechanism of resistance to single-agent targeted therapy in these tumours, and suggest a novel combinatorial treatment strategy to overcome it in the clinic.

3

INTRODUCTION

The mitogen-activated protein kinase (MAPK) pathway plays an important role in signal transduction regulating cell proliferation, differentiation and cell death (1). Dysregulation of the MAPK signalling pathway is implicated in a wide range of cancers as a result of genetic and epigenetic alterations. In adults, *BRAF* mutated tumours include 60% of melanomas, 60% of thyroid cancers, 15% of colorectal and 5-8% of non-small cell lung cancer, with the most prevalent mutation being *BRAF*_V600E (2). In addition, non-V600E mutations have been identified to be oncogenic and can be classified as one of three types based on their effect on BRAF activity (3,4).

MAPK pathway alterations are commonly found in childhood cancer, particularly brain tumours, and especially low and high-grade gliomas (5). These include pilocytic astrocytoma (*KIAA1549:BRAF* tandem duplication, *RAF* fusions, *NF1*, *FGFR1*, *BRAF*_V600E) (6,7), mixed glioneuronal tumours (*FGFR1, BRAF*_V600E, *KIAA1549:BRAF*) (8-10), pleomorphic xanthoastrocytomas (*BRAF*_V600E) (11,12), infant pHGG (*NTRK1/2/3, ROS1, ALK, MET* fusions) (13-15), non-brainstem pHGG (*FGFR1, NF1*, *BRAF*_V600E, *NTRK2*_ITD*, MET*) (13,16-18) and DIPG (*PIK3R1, NF1*) (13,19). For the latter, with a median survival of 9-12 months (20), they represent an unexplored option in a tumour type in desperate need of novel treatment strategies (21).

Although targeted agents against the MAPK pathway have become an important initial success story in the field of precision oncology, they are frequently associated with the emergence of resistance and treatment failure (22). Therapy-induced resistance can occur from the acquisition of *de novo* mutations (23,24) or from expansion of rare pre-existing resistant cells, also called "persister clones" (25-27). The use of inhibitors such as those targeting BRAF (vemurafenib, dabrafenib) and MEK (trametinib, selumetinib, cobimetinib), in *BRAF*_V600E positive melanoma resulted in a moderate success of targeted therapies by showing tumour shrinkage and improving patient survival (28-30). However, durable responses were limited, due to resistance to single-agents often mediated by re-activation of

4

MAPK through amplification or splice variants in *BRAF*, mutations in the upstream oncogene *NRAS* or the downstream kinase *MEK1* (*MAP2K1*)*,* as well as PI3K-PTEN-AKT upregulation, amongst others (24,31-34). This led to the combination of BRAF and MEK inhibitors in clinical trials which showed a significant improvement in overall survival compared to single agent therapy and subsequently FDA-approved treatment for advanced *BRAF*_V600E positive melanoma (35,36). However, acquired resistance was observed in patients under BRAF and MEK inhibitors, with the identification of *MEK1* and *MEK2* (*MAP2K2*) mutations as two of the main mechanisms (31,37-40).

Despite their clinical availability for treating children with brain tumours harbouring targetable alterations (41,42), BRAF and MEK inhibitors have thus far not been explored in DIPG. As part of a co-clinical trial of DIPG patients from the UK enrolled in BIOMEDE, an adaptive, international, phase II clinical trial in newly diagnosed DIPG (NCT02233049), we have generated patient-derived *in vitro* and *in vivo* models subjected to integrated drug screening and molecular profiling. We identify specific genetic dependencies associated with response to trametinib *in vitro*, explore mechanisms of acquired resistance which emerge to single agent targeted therapy which emerge, and present rational drug combinations which may circumvent this in future clinical trials.

5

RESULTS

MAPK alterations confer in vitro sensitivity to trametinib in DIPG models from a co-clinical trial

BIOMEDE (NCT02233049) was a phase II, biopsy-driven clinical trial in DIPG patients with randomisation of stratification between dasatinib, erlotinib and everolimus. From UK patients, we undertook to generate patient-derived *in vitro* and *in vivo* models from biopsy material excess to trial inclusion. From the first 12 cases, exome sequencing was performed on the biopsy specimen itself, and panel sequencing performed on the *in vitro* cultures established under stem cell conditions in 2D (on a laminin matrix) and 3D (as neurospheres), as well as tumours grown as orthotopic xenografts in mice (Figure 1A). Seven cases presented with *H3F3A* (now *H3-3A*) K27M mutations, one had *HIST2H3C* (now *H3C14*) K27M, and another presented *EZHIP* overexpression by RNA sequencing, recently described as phenocopying the H3K27M mutation-driven loss of H3K27me3 (43). Of the three histone H3 wild-type cases, one harboured *MYCN/ID2* co-amplification. Recognised recurrent DIPG driver mutations were largely preserved between the biopsy and models, with specific exceptions between 2D and 3D cultures described below, and some amplicons (*PDGFRA, MYCN*) discrepant between different samples from the same patient (Figure 1A). Similarly, all models were highly concordant with their original tumours on the basis of their methylation profiles derived from Illumina 850K EPIC arrays (Figure 1B). Although all *H3F3A*_K27M and *EZHIP* cases clustered with other diffuse midline glioma (DMG) K27M tumours, the *HIST2H3C*_K27M case (ICR-B184) was most similar to ICR-B118 and other MYCN-amplified glioblastoma in the t-SNE projection of the methylation array data (Figure 1B). The H3 wild-type case ICR-B128 did not classify strongly with any known subgroup. A summary of the molecular data of the models and the tumours from which they were derived is given in Supplementary Table S1.

17 established cultures from 11 patients were subjected to a drug mini-screen against a range of targeted inhibitors (n=13), selected on the basis of their molecular profiles (Figure 1C). Exploring these data for genetic dependencies, we observed a striking concordance of mutations in the MAPK pathway (*BRAF*, *NF1*, *PIK3R1*) and sensitivity to the MEK inhibitor

6

trametinib, both in 2D and 3D, including the models ICR-B169 in 2D (Figure1D), and ICR-B169, ICR-B181 and ICR-B184 in 3D (Figure 1E).

Functional selection of MAPK alterations in model systems and translation to the clinic

ICR-B181 harboured a subclonal (VAF=18%) hotspot mutation in *PIK3R1*, N564D (Figure 2A). ICR-B184 was found to have a subclonal (VAF=20%) frameshift mutation in *NF1* in the biopsy (E78fs) that was absent from the models, which instead presented the missense mutation I1824S (Figure 2B). In both cases, the likely MAPK-activating mutations were only observed in the 3D cultures, not the 2D, which corresponded with a marked increase in sensitivity to trametinib in the neurospheres compared to adherent cells, when validated in a full dose-response analysis (~420-fold for ICR-B181 (Figure 2C); and ~460-fold for ICR-B184 (Figure 2D), p<0.0001 AUC t-test). Similar results were observed with the additional MEK inhibitors cobimetinib (10-fold for ICR-B181, p=0.0012 AUC t-test (Supplementary Figure S1A); and 28-fold for ICR-B184, p=0.0004 AUC t-test (Supplementary Figure S1B)) and binimetinib (6-fold for ICR-B181, p=0.0035 AUC t-test (Supplementary Figure S1C); and 18-fold for ICR-B184, p=0.0007 AUC t-test (Supplementary Figure S1D)).

Using a quantitative capillary phospho-protein platform, we observed ~2-fold higher basal levels of MAPK pathway activation (phospho-ERK1/2$^{T202/Y204}$) in the mutant 3D compared to wild-type 2D cultures for both cell models (Figure 2E). Notably, the *PIK3R1*_N564D mutation was present in both 2D (36/227 reads, VAF=16%) and 3D (100/301 reads, VAF=33%) cultures of ICR-B181 at passage 5, whereas it was completely absent from the laminin culture at passage 18 (0/342 reads), whilst presumably clonally heterozygous in the neurospheres (195/396 reads, VAF=49%). These positive and negative selections in culture was confirmed over sequential passages by a bespoke ddPCR assay (Figure 2F)(Supplementary Table S2). By contrast, the *NF1*_I1824S mutation was never observed in the ICR-B184-2D cultures (0/201 reads at passage 4). Remarkably, orthotopic engraftment of ICR-B181-2D (p18, 20/5476 *PIK3R1*_N564D droplets, VAF=0.32% (Supplementary Figure S1E) failed to produce

7

tumours after 12 months, whilst implantation of ICR-B181-3D (p17, 4919/9727 *PIK3R1*_N564D droplets, VAF=50.6% (Supplementary Figure S1F) gave rise to in 10/10 NSG mice with a median overall survival of 310 days (Figure 2G), producing diffusely infiltrative tumours (Figure 2H) visible on MRI (Figure 2I) and histologically consistent with a high grade glioma (Figure 2J).

ICR-B169 (2D and 3D) harboured a clonal, heterozygous, non-canonical class II *BRAF* oncogenic mutation, G469V (Figure 3A). Following feedback of our molecular and *in vitro* drug screening data, the patient was clinically treated with trametinib on a compassionate use basis (0.025 mg/kg/day once daily, the paediatric recommended phase II dose previously established in an international phase I/II clinical trial), two months after progression at 16 weeks on everolimus and radiotherapy. During 11 weeks on trametinib, the patient improved clinically, was able to be taken off the steroid treatments required over the previous 3 months, and showed radiologically stable disease during this time. However, an MRI at week 12 showed progression with the appearance of new metastatic lesions within the brainstem and in the lateral ventricles, and the patient died from disease shortly afterwards (Figure 3B). In parallel, mice bearing orthotopic xenografts derived from ICR-B169 cells (3D) were treated with trametinib from day 55 post-implantation, 1 mg/kg orally once daily over 53 days (5 days on, 2 days off). No difference in overall survival between trametinib and vehicle-treated animals was observed (p=0.7123, log-rank test) (Figure 3C).

MEK1/2 mutations drive resistance to trametinib in BRAF_G469V-driven DIPG cells

As trametinib single agent did not achieve the expected efficacy both *in vivo* and clinically we sought to explore the mechanisms by which resistance to MEK inhibition may occur in DIPG, and identify strategies to circumvent these. We first attempted to generate subclones of ICR-B169 cells resistant to trametinib by two continuous exposure approaches *in vitro*, the first by an exponential increase in drug concentration from the GI_{50} value over time, and the second by a constant GI_{80} dose (Figure 3D). Both experiments produced subclones with increasing

8

resistance to trametinib, with shifts in GI_{50} values over 5-9 months of 64 to 167-fold with the exponential model (Supplementary Figure S2A), and 5 to 56-fold with the constant GI_{80} approach (Supplementary Figure S2B). To explore what might be underlying the lack of sensitivity in selected subclones, exome sequencing was carried out in the most resistant cells, compared to both the original tumour biopsy and the parental ICR-B169 cells. Strikingly, all three clones were found to contain mutations in either *MEK1* (K57N or I141S) or *MEK2* (I115N) (Supplementary Figure S2C). The three models chosen for further work were 46- (T1, *MEK2*_I115N), 101- (T3, *MEK1*_I141S), and 33-fold (T6, *MEK1*_K57N) more resistant to trametinib than parental cells (p=0.0003-0.0008, AUC t-test) (Figure 3E), a phenotype maintained after the inhibitor was withdrawn for two months (p=0.0003-0.0096, AUC t-test) (Figure 3F), as were the *MEK1/2* mutation VAFs (T1 *MEK2*_I115N, 12% to 14.6%; T3 *MEK1*_I141S, 28.2% to 30.5%; T6 *MEK1*_K57N 26% to 24.9%). Compared to the parental cells, the resistant clones required 10-100-fold higher concentrations of trametinib to effectively inhibit phospho-ERK1/2, as measured by quantitative capillary phospho-protein analysis (Supplementary Figure S2D).

To evaluate if resistance was selected from pre-existing tumour subclones or was acquired *in vitro* in response to trametinib, allele-specific ddPCR assays for the *MEK1/2* mutations were conducted in both the original tumour biopsy and the parental cells (Supplementary Figure S3A). No mutant droplets were found in either sample for any of the three mutations, with an average number of wild-type droplets of 32,165 and 41,083 respectively. We additionally found no *MEK1/2* mutant droplets in either vehicle or trametinib-treated CDX specimens from our earlier efficacy experiment. Exome sequencing of these latter specimens confirmed the lack of *MEK1/2* mutations, however in 4/5 treated mice, we observed plausible variants in genes which converge on RAF/MEK signalling, including *MYBL1*, *IRAK1*, *DUSP26* and others (Supplementary Figure S3B), highlighted by STRING protein-interaction analysis (Supplementary Figure S3C).

The trametinib-resistant clones were also cross-resistant to the additional MEK inhibitors cobimetinib (p<0.0001-0.0004 AUC t-test) (Supplementary Figure S4A) and binimetinib (p=0.0021-0.0033 AUC t-test) (Supplementary Figure S4B), with GI50 values not reached at 10μM drug. When implanted orthotopically in immune-deficient mice, they had a substantially longer latency time to tumour formation as seen with median survival times of 225-435 days, compared with the 185 days of the ICR-B169 parental (Supplementary Figure S4C) .

The allele-specific *MEK1/2* ddPCR assays were further used to track the emergence of *MEK1/2* mutations from longitudinal passages over the course of the continuous exposure experiments. Under both experimental conditions, *MEK1/2* VAF increased in an exponential manner over time, however an earlier emergence was observed in the clone exposed to constant GI_{80} trametinib concentration (T6 *MEK1*_K57N) (Figure 3G). This increase in *MEK1/2* mutation frequency was mirrored by the increasing GI_{50} values over sequential passages (Figure 3H). In all three resistant models, *MEK1/2* mutations conferred an enhanced constitutive MAPK pathway activation by quantitative capillary phospho-protein analysis. This was, however, read out at different nodes in the pathway with different *MEK1/2* mutations, with T1 *MEK2*_I115N showing enhanced phospho-MEK1/2$^{P217/P221}$ (p<0.0001), T3 *MEK1*_I141S increased phospho-AKT^{S473} (p=0.0166) and phospho-P90/RSK^{S380} (p=0.0096) and T6 *MEK1*_K57N higher phospho-ERK1/2$^{P202/P204}$ (p=0.0006) and phospho-AKT^{S473} (p=0.0074, all one-way ANOVA) (Figure 3I).

Mechanisms of MEK1/2 mutation-driven resistance to trametinib

To explore the mechanism by which mutations in *MEK1/2* confer resistance to trametinib in DIPG cells, we carried out gene expression profiling by RNA-seq, as well as total and phospho-proteome analysis by LC-MS/MS in our resistant clones. We identified 277, 127 and 241 differentially up-regulated, and 232, 175 and 214 down-regulated genes at the transcript level in T1, T3 and T6 respectively, compared to ICR-B169 parental cells (Supplementary Figure S5A). Of those, a total of 41 genes were shared to be up-regulated and 56 genes to be

10

down-regulated amongst the three clones (Supplementary Figure S5B,C). From the total proteome, 447, 378 and 435 proteins were differentially over-expressed and 626, 673, 729 under-expressed in the clones (Supplementary Figure S5D), with 137 and 225 respectively in common between the three clones (Supplementary Figure S5E,F). Phospho-proteomics identified a total of 212, 37 and 167 phospho-peptides from 124, 22 and 106 proteins with increased phosphorylation and 561, 171 and 395 phospho-peptides from 373, 117 and 221 proteins with decreased phosphorylation in T1, T3 and T6 respectively (Supplementary Figure S5G). Of these, a total of 8 proteins with increased phosphorylation and 57 with decreased phosphorylation were shared amongst the three clones (Supplementary Figure S5H,I).

The intersection of the shared most differentially up-regulated (n=28, Figure 4A) or down-regulated (n=24, Figure 4B) genes, proteins, and phospho-sites between any of the three clones resulted in an integrated signature of co-ordinately regulated signalling changes induced by *MEK1/2* mutation in response to challenge by trametinib treatment. Gene set enrichment analysis (GSEA) of this integrated signature showed a high degree of concordance between the clones (Supplementary Figure S6A,B), and included activation of numerous processes involved with cytoskeleton re-organisation, cell migration, cell polarisation, and cell matrix remodelling, as well as depletion of neural and oligodendrocyte markers. Consequently, there was a highly significant under-representation of such differentiation profiles such as the VERHAAK_GLIOBLASTOMA_PRONEURAL signature in the clones (nominal p value = 0.000446) (Figure 4C), along with an enrichment of mesenchymal gene sets such as HALLMARK_EPITHELIAL_MESENCHYMAL_TRANSITION (nominal p value = 0.000227) (Figure 4D). Most notably, there was also a significant enrichment of a gene signature indicative of sensitivity of cancer cells lines to dasatinib, HUANG_DASATINIB_RESISTANCE_UP (nominal p value = 0.000337) (Figure 4E) (Supplementary Table S3).

Combinatorial approaches for overcoming trametinib resistance in DIPG

In considering opportunities for how to effectively treat MAPK-driven DIPG cells which have become resistant to MEK inhibitors, we first tested the downstream ERK inhibitor ulixertinib, as reported in other tumour types (44,45). No differences in sensitivity were observed between T1 *MEK2*_I115N or T3 *MEK1*_I141S and the ICR-B169 parental cells, whilst T6 *MEK1*_K57N cells were significantly less sensitive to ulixertinib (p=0.0024, AUC t-test) (Figure 5A). By contrast, treatment with the upstream RTK inhibitor dasatinib revealed a marked differential sensitivity in all trametinib-resistant clones, with a 68 to 174-fold shift in GI_{50} values (p=0.009-0.0004, AUC t-test) (Figure 5B). With this reciprocal potency of trametinib and dasatinib in the ICR-B169 parental cells and subclones, we next investigated whether this was true in all the patient-derived culture we initially assessed. Cells classed as trametinib resistant in the mini-screen were found to have significantly lower GI_{50} values for dasatinib than the trametinib-sensitive cultures (p=0.0017, unpaired t-test) (Figure 5C), whilst the converse was also true; dasatinib sensitive cells had significantly higher GI50 values for trametinib than those classed as dasatinib-resistant (p=0.0014, unpaired t-test) (Figure 5D).

Given the similarities between a range of distinct patient-derived cultures (and their relative responses to trametinib), and the resistant clones generated from the *BRAF*_G469V-driven ICR-B169 cells, we applied GSEA to the RNA-seq data on the panel of untreated *in vitro* models. There was substantial overlap in the significantly differentially expressed gene signatures observed in the inherently trametinib-resistant primary cultures, and those seen in the *MEK1/2*-mutant resistant ICR-B169 clones (Supplementary Figure S6C). Most strikingly, there was a highly significant under-representation of the VERHAAK_GLIOBLASTOMA_PRONEURAL signature in the inherently trametinib-resistant cultures (nominal p value = 0.000231), significantly enriched in dasatinib-resistant cells (nominal p value = 0.000204) (Figure 5E), along with the reverse pattern for mesenchymal gene sets such as HALLMARK_EPITHELIAL_MESENCHYMAL_TRANSITION (trametinib-resistant, nominal p value = 0.000172; dasatinib-resistant, nominal p value = 0.000196)

12

(Figure 5F). As expected, we also observed a significant enrichment in the inherently trametinib resistant cells, and under-representation in the dasatinib-resistant primary cultures, of the HUANG_DASATINIB_RESISTANCE_UP gene set (nominal p value = 0.000184 and nominal p value = 0.000198, respectively) (Figure 5G) (Supplementary Table S3). As dasatinib is a multi-targeted kinase inhibitor, we explored which of these may underlie the response in the trametinib-resistant cells by phospho-protein array profiling. In T6 (*MEK1*_K57N) cells, we observed only a modest decrease in p-PDGFRB^{Y571} (Supplementary Figure S6D) and p-AKT^{S473} (Supplementary Figure S6E) in response to dasatinib at the higher doses. By contrast, there were high basal levels of p-SRC^{Y419} (Supplementary Figure S6F) and pYES1^{Y426} (Supplementary Figure S6G), which were dramatically inhibited at the lowest doses of dasatinib, correlating with the cellular response (Supplementary Table S4). Notably, there was also a specific shift in dasatinib sensitivity in the paired ICR-B181-2D and -3D (*PIK3R*1_N546D) cells (3-fold, p=0.0398 AUC t-test) (Supplementary Figure S6H), as well as the ICR-B184-2D and -3D (*NF1*_I1824S) cells (7.7-fold, p=0.0012 AUC t-test) (Supplementary Figure S6I).

Finally, we assessed whether this reciprocal sensitivity to targeted inhibition would lead to an effective combination therapy in MAPK-driven DIPG cells. We used the BLISS independence model to assess the combination of dasatinib and trametinib, which showed profound effects on cell viability in ICR-B169 parental cells, even at low doses of both drugs (Figure 6A). This was in contrast to the trametinib-resistant clones, which unsurprisingly required high levels of MEK inhibitor to produce an effect (large black areas on heatmap). This was more formally evaluated by calculating the excess above BLISS scores for each pairwise combination, identifying likely synergistic areas within the combinatorial matrix, highlighted in red on the heatmap (Figure 6B). A summary synergy score was calculated as the average excess response due to drug interactions above expectations, with the resulting value of 19.9 in the ICR-B169 parental cells indicating a high degree of formal synergy at the lowest doses of trametinib, an effect not seen in the resistant clones, in an analogous pattern to the cell viability

13

score above (Figure 6C). Notably, there was also a highly synergistic interaction of ulixertinib and trametinib in both parental and resistant clones, particularly with the T6 *MEK1*_K57N cells, which were largely resistant to ulixertinib as a single agent (Supplementary Figure S7A-C).

In order to validate our proposed combinatorial approach, we established mouse *ex vivo* brain slice cultures, onto which we implanted ICR-B169 parental cells (Figure 7A). Treatment with the combined trametinib and dasatinib resulted in a significantly reduced growth capacity across the brain parenchymal tissue compared to vehicle (p=0.0003, FDR-corrected t-test), or either agent alone (p=0.0057 vs dasatinib; p=0.050 vs trametinib; FDR-corrected t-test) (Figure 7B). Critically, there was a substantial reduction in cell number evident in the tumour cell core in the combination arm not observed with the single agents.

Thus, we present evidence for a subset of DIPG patients to harbour MAPK pathway activating mutations, sensitivity to MEK inhibition *in vitro* with the rapid acquisition of consistent resistance mutations, and identify potentially efficacious combination approaches based upon the common mechanisms underlying these events.

DISCUSSION

In the setting of a co-clinical trial of prospectively-established DIPG patient-derived models, we show the identification of biomarkers of response to trametinib, a selective reversible inhibitor of MEK1/2 that binds to the allosteric pocket of MEK. Specifically, these involve multiple nodes of the MAPK signalling pathway, and include *PIK3R1*_N564D, *NF1*_I1824S and *BRAF*_G469V. These results suggest a possible rationale for the use of trametinib in DIPG, such as the ongoing phase II clinical trial called TRAM-01 (NCT03363217), which is exploring the use of trametinib in paediatric gliomas harbouring MAPK alterations independently of the tumour entity (46).

*PIK3R1*_N564D is an oncogenic hotspot mutation known to promote cell survival *in vitro* and oncogenesis *in vivo* (47), and lies within the regulatory subunit of PI3-kinase resulting in loss-of-function, predicted to destabilise protein interaction which may impact tumour suppressive function (FATHMM pathogenic score of 0.99) (48,49). Such *PIK3R1* oncogenic mutations have been shown to activate the MAPK pathway and exhibited sensitivity to MAPK inhibitors (50). *NF1*_I1824S lies in the neurofibromin chain and the lipid binding region, which may affect the protein folding and the tumour suppressor gene function (48); it has also been reported in a patient with neurofibromatosis type 1 (51), and is absent from population databases. The efficacy of MEK inhibitors has previously been shown in NF1-deficient glioblastoma cell lines (52), in addition to clinical benefit in refractory neurofibromatosis-associated glioma harbouring *NF1* mutation (53-55). By stochastic selection, an imbalance of variant allele frequency between 3D and 2D cultures from the same patient was observed in ICR-B181 (*PIK3R1*_N564D) and ICR-B184 (*NF1*_I1824S). Trametinib sensitivity was only identified in the mutant cultures, which also had higher basal levels of MAPK pathway activation, which would support the hypothesis that these mutations were responsible for the observed trametinib efficacy *in vitro.*

*BRAF*_G469V is a class II *BRAF* mutation within the protein kinase domain, resulting in increased kinase activity and downstream MEK and ERK activation (3). *BRAF* class II

15

mutations have constitutively activated BRAF dimers independent of RAS activation (3), and *BRAF*_G469V has been shown to confer sensitivity to trametinib in melanoma and lung cancer (4,56). Despite this, in the context of DIPG, targeting this mutation with MEK inhibitor as a single agent *in vivo* and clinically failed to elicit a significant response. Although there may be issues with the treatment regimen used in our long-latency orthotopic xenografts, and the patient received trametinib only post-progression after several months on everolimus and radiation, there are also concerns over the emergence of resistance to MEK inhibition as previously described in melanoma or colorectal cancers (37-40). Such a process we showed to be active in DIPG cells through the acquisition in continuous exposure experiments *in vitro* of *MEK1/2* mutations, resulting in pathway re-activation and the irreversible resistance to trametinib. Although not observed in trametinib-insensitive CDX models *in vivo*, we did observe plausible variants which form part of a BRAF-MEK1/2 circuit, further underlying the importance of reactivation of this element of the signalling pathway in response to drug interventions.

MEK1 and MEK2 exhibit 85% peptide sequence homology (57). *MEK1*_K57N lies on the helix-A domain within the N-terminal negative regulatory region and is associated with high levels of RAF-regulated activation of ERK signalling (31,58). Interestingly, *MEK1*-K57N has been attributed to cause resistance to BRAF and MEK inhibitors *in vitro* and in melanoma patients (45,59). To the best of our knowledge, neither *MEK1*_I141S nor *MEK2*_I115N have been previously detected, although both mutations lie within the protein kinase domain affecting the allosteric pocket (45). Particularly, *MEK1*_I111N, the equivalent of *MEK2*_I115N, has been demonstrated to confer resistance *in vitro* to allosteric MEK inhibitors (31,45). In our resistant clones, presence of the *MEK1/2* mutations resulted in shift of 2-3 orders of magnitude of trametinib concentration required to inhibit MAPK signalling.

Notably, using integrated RNA-seq and phospho-/total proteomics, a drift from a proneural to a mesenchymal phenotype was observed in the *MEK1/2*-mutant resistant clones, a feature also observed in patient-derived models inherently insensitive to trametinib. This has been

broadly reported as a hallmark of metastasis and resistance to multitherapy in cancer (60,61). In particular, glioma-initiating clones displaying drug resistance and radio-resistance have been previously linked to a proneural-mesenchymal transition (62). In our models, this was also accompanied by a reciprocal sensitivity of the trametinib-resistant DIPG cells to the multi-kinase inhibitor dasatinib. In this context, phospho-kinase profiling highlighted Src-family kinases as the likely mediators of this response rather than PDGFR signalling. In other cancers, a proportion of *KRAS*-mutant cell lines resistant to trametinib were found to have a mesenchymal gene expression signature (63), and dasatinib has been reported to overcome mesenchymal transition-associated resistance to erlotinib in non-small cell lung cancers (64). In addition, a study has found that dasatinib sensitises *KRAS*-mutant cancers to trametinib both *in vivo* and *in vitro* (65). In DIPG, the combined use of dasatinib and trametinib showed a high degree of synergy *in vitro* and on *ex vivo* brain slices and may represent a novel combinatorial approach in this disease.

It remains to be explored how best these combinations could be translated clinically in order to prevent or overcome resistance to MEK inhibitors. Critically, we observed consistent results in our primary patient-derived cultures, 2D/3D MAPK-altered isogenic cells, and the trametinib-resistant clones for the more clinically relevant brain-penetrant MEK inhibitors cobimetinib and binimetinib. Going forward, assessment of an intermittent multitherapy regimen to control population dynamics and potentially prevent emergence of treatment resistance to begin with is clearly warranted. In this context, mathematical modelling and adaptive drug design will be essential to determine treatment scheduling, exploiting the fitness trade-offs associated with resistance therapy (66).

17

ACKNOWLEDGEMENTS

18

AUTHOR CONTRIBUTIONS

CJ, EI, DC and AM conceived the study. EI, DC and ARF established *in vitro* cultures. DC carried out *in vivo* work. JB and SPR performed *in vivo* MRI and analysis. GP, MAA-C and MV carried out the *ex vivo* brain slice experiments. EI, DC, EFP, MD, RR and MS carried out drug screening; EI performed drug resistance experiments. EI, PP, ST carried out molecular profiling. EI, YG, AM and MH carried out bioinformatic analysis. DC and MD performed phospho-protein profiling; LY, GR and JC carried out full proteome and phospho-proteome analysis. VM carried out IHC. TSJ, RG, LH, SP, JA, SW, JG, BZ, LVM, FC, JG, DH, SD and POH provided samples and clinical annotation. EI and CJ wrote the manuscript.

19

METHODS

Primary patient-derived cell cultures

DIPG biopsy tissue was shipped to our laboratory either in Hibernate A transport media (ThermoFisher Scientific, A12475-01) at room temperature, or minced with a sterile scalpel blade in DMEM/F12 (Life Technologies, 11320-074) supplemented with 0.2% BSA (Sigma-Aldrich, A1595) and 10% DMSO (Sigma-Aldrich, D2650), frozen at -80°C and sent on dry ice. (Supplementary Table S1). Minced tissue was digested using Liberase DL. Supernatant was removed and the tissue/cells were resuspended in stem cell media and continuously pipetted to ensure dissociation, before transfer to culture flasks either to grow either attached on a laminin substrate (Merck Millipore, CC095) and/or in suspension as neurospheres in ultra-low attachment flasks (Sigma-Aldrich, CLS3815). The cells were grown at 37°C, 5% CO2 in stem cell media consisting of Dulbecco's Modified Eagles Medium: Nutrient Mixture F12 (DMEM/F12; Life Technologies, 11330-038), Neurobasal-A Medium (Life Technologies, 10888-022), HEPES Buffer Solution 1M (Life Technologies, 15630-080), MEM Sodium Pyruvate Solution 100 nM (Life Technologies, 11360-070), MEM Non-Essential Amino Acids Solution 10 mM (Life Technologies, 11140-050) and Glutamax-I Supplement (Life Technologies, 35050-061). The media was supplemented with B-27 Supplement (Life Technologies, 12587-010), 20 ng/ml recombinant Human-EGF (2B Scientific LTD, 100-26), 20 ng/ml recombinant Human-FGF (2B Scientific LTD, 100-146), 20 ng/ml recombinant Human-PDGF-AA (2B Scientific LTD, 100-16), 20 ng/ml recombinant Human-PDGF-BB (2B Scientific LTD, 100-18), and 2 µg/ml Heparin Solution (Stem Cell Technologies, 07980).

Nucleic acid extraction

DNA and RNA were isolated from the same piece of tissue or cell pellet by using ZR-Duet DNA/RNA Miniprep Plus (Zymo Research, D7001). If only DNA was extracted, DNeasy Blood & Tissue Kit (Qiagen, 69581) was used and if only RNA was extracted, Rneasy Mini Kit protocol (Qiagen, 74104) was used. DNA and RNA quality were measured using Nanodrop

20

spectrophotometer (Thermo-scientific). DNA concentration was determined using Qubit fluorometer (Thermo Fisher Scientific, Q32850 and Q32851). RNA integrity was analysed and quantified using 4200-Tapestation (Agilent).

Whole exome sequencing

Libraries were prepared from 50-200 ng of DNA using the Kapa HyperPlus kit and DNA was indexed utilising 8bp-TruSeq-Custom Unique Dual Index Adpaters (IDT). Libraries were pooled in 8-plex, (2500-500 ng of each library), by equal mass and normalised to the lowest mass sample. Samples were then hybridised overnight (16-18 hours) with the xGen Exome Research panel v1 (IDT) and sequenced on an Illumina NovaSeq 6000 system using the S2-200 Reagent kit (Illumina, 20012861) or the SP Reagent kit (Illumina, 20027465). Capture reads were aligned to the GRCh37/Hg19 build of the human genome using bwa bwa v0.7.12 (bio-bwa.sourceforge.net), PCR duplicates were removed with PicardTools 1.94 (pcard.sourceforge.net) and BEDTools was used for quality control (QC) and generation of metrics for each sample. Single nucleotide variants were called using the Genome Analysis Tool Kit v3.4-46 based upon current Best Practices using the Unified Genotyper (broadinstitute.org/gatk/). Variants were annotated using the Ensembl Variant Effect Predictor v74 (ensembl.org/info/docs/variation/vep) incorporating SIFT (sift.jcvi.org) and PolyPhen (genetics.bwh.harvard.edu/pph2) predictions, COSMIC v64 (sanger.ac.uk/ genetics/CGP/cosmic/), dbSNP build 137 (ncbi.nlm.nih.gov/sites/SNP), ExAc and ANNOVAR annotations. Copy number was obtained by calculating $\log_2$ ratios of tumour/normal coverage binned into exons of known Ensembl genes, smoothed using circular binary segmentation (DNAcopy, www.bioconductor.org) and processed using in-house scripts in R. Interaction networks were analysed and visualised by STRING (string-db.org).

RNA sequencing

At least 150 ng of RNA was sequenced at Eurofins Genomics. Strand-specific cDNA libraries were made by purification of poly-A containing mRNA molecules follow by mRNA

21

fragmentation and random primed cDNA synthesis (strand specific). Adapter ligation and adapter specific PCR amplification was performed before sequencing on Illumina sequencers (Hiseq or Novaseq) using 150 bp paired-end reads chemistry according to the manufacturer's instructions. RNAseq data was aligned with STAR and summarized as gene level fragments per kilobase per million reads sequenced using BEDTools and HTSeq. Following rlog transformation and normalization, differential expression was assigned with DESeq.2. Fusion transcripts were detected using chimerscan ver 0.4.5a filtered to remove common false positives. Gene set enrichment analysis was carried out using the R package fastGSEA (fGSEA) based upon curated canonical pathways (MsigDB, Broad).

Methylation

A total of 50-500 ng of DNA was bisulphite-modified using the EZ DNA Methylation-Direct kit (Zymo, D5006), loaded onto the Illumina Infinium MethylationEPIC BeadChip and the array intensities were read on the Illumina iScan system at the University College London Genomics Centre, according the manufacturer's instructions. Methylation data from the Illumina Infinium HumanMethylation850 BeadChip was pre-processed using the minfi package in R (v11b4). DNA copy number was recovered from combined intensities using the conumee package. The Heidelberg brain tumour classifier (67) (molecularneuropathology.org) was used to assign a calibrated score to each case, associating it with one of the 91 tumour entities which feature within the current classifier. Clustering of beta values from methylation arrays was performed based upon correlation distance using a ward algorithm. DNA copy number was derived from combined $\log_2$ intensity data based upon an internal median processed using the R packages minfi and conumee to call copy number in 15,431 bins across the genome.

ddPCR

Custom TaqMan-based quantitative PCR genotyping assays (Applied Biosystem, Thermo Scientific) were designed to specifically detect *PIK3R1*-N564D and *MEK1*-K57N, *MEK1*-I141S and *MEK2*-I115N mutations (Supplementary Table S2). ddPCR was performed by using the

Bio-Rad automated droplet generator (BioRad, QX200 AutoDG), and the Bio-Rad QX200 droplet reader, based on the manufacturer's guidelines. Results were analysed using Bio-Rad QuantaSoft Analysis Pro software. At least two single FAM-positive droplets were required to call a sample positive.

Drug assays

Primary cells were incubated in 96- or 384-well plates for three days before adding the compounds with serial dilution at ten different concentrations and eight days later, (end-point, day 11) cell viability was measured using CellTiter-Glo (2.0, or 3D assays as appropriate, Promega). Relative luminescence units (RLU) for each well was normalised to the median RLU from the DMSO control wells as 100% viability. At least two duplicates per drug condition were performed as well as a minimum of three independent biological replicates. GI50 values (drug concentration causing 50% inhibition of cell proliferation) were calculated using GraphPad Prism and the curves show the mean ± standard error of the replicates per condition measured. All the compounds were purchased from Selleckchem except for CUDC-907 and PTC-209 which were obtained from Apexbio. The compounds were diluted in DMSO to a final concentration of 10 mM. Drug plates were prepared using the acoustic liquid handler Echo 550 (Labcyte). Each plate included six compounds at eight different concentrations as well as a cytotoxic chemotherapeutic (camptothecin) as positive control, as well as DMSO as a negative control. Drug combinations were assessed by adding one compound in rows and another in columns with serial dilutions resulting in a 6 x 10 dose matrix using different fold dilutions manually prepared. The stand-alone web-application SynergyFinder (https://synergyfinder.fimm.fi) was used for interactive analysis and visualization of multi-drug combination profiling data following the Bliss independence model (68,69).

Generation of resistant clones

ICR-B169 resistant clones were established by culturing the parental line in escalating concentrations of trametinib from 0.05 µM (GI50) to 1 µM in an exponential stepwise manner,

23

or by exposing the cells to a constant concentration of trametinib of 0.5 μM (GI80 value). Both methods were performed using two technical replicates and two independent biological replicates for a total of eight derived cultures plus four replicate control flasks which were treated with the same concentration of DMSO in parallel to the establishment of the resistant cells. Cells were maintained in DMSO only for two passages to keep the baseline clonal population as close as possible to the parental culture. A total of $1\text{-}1.4\times10^6$ cells were seeded in a T75 flask for the resistance assay and 2-3 days later the media with trametinib was added at the appropriate concentration or DMSO to the control flasks. For the escalating-dose approach, ten different concentrations were used with an exponential increment and the same dose was added a total of 6 times. During the generation of resistance, the stem cell media containing the drug or DMSO was replaced three times a week and the cells split when they reached 90% confluency.

Capillary-based protein quantification

Cells were scraped from the flask and collected in media or cold PBS, and then centrifuged at 1,300 rpm for 5 min, resuspended in 1 ml of cold PBS and centrifuged at 4,000 rpm for 4 min. The supernatant was then removed and the pellet was resuspended in 50-100 μl cold lysis buffer (Cell Signalling Technologies, 9803) containing protease inhibitor cocktail mini-tablet (Roche, Diagnostics, 11836153001) and phosphatase inhibitors (Sigma-Aldrich, P044 and P5726). Lysates were sonicated for 10 sec at 40% amplitude, spun at 14,000 rpm for 10 min in a cold microfuge and quantified using BCA Protein Assay Kit (Thermo-Fisher, 23225). Capillary electrophoresis was conducted using the automated Wes system (ProteinSimple) with the 12-230 kDa Separation module (SM-W004) and the anti-rabbit detection module (DM-001) following the manufacturer's instructions, and analysed with Compass software. The following primary antibodies were used: AKT (1:50, Cell Signalling Technologies, 9272), phospho-AKT^{Ser473} (1:50, Cell Signalling Technologies, 4060), ERK1/2 (1:100, Cell Signalling Technologies, 9102), phospho-ERK$^{T202/Y204}$ 1:100 (Cell Signalling Technologies, 9101), MEK1/2 (1:50, Cell Signalling Technologies, 9122), pMEK1/2$^{S217/221}$ (1:50, Cell Signalling

24

Technologies, 9121), α-Actin (1:200, Cell Signalling Technologies, 6487) and the AKT/MAPK pathway antibody cocktail (1:25, Abcam, 151279). Goat Anti-Rabbit HRP conjugate (Protein Simple, 042-206) was used as a secondary antibody.

Phospho-kinase profiling

Capillary electrophoresis was conducted using the automated Wes system (ProteinSimple) with the 12-230 kDa Separation module (SM-W004) and the anti-rabbit detection module (DM-001) following the manufacturer's instructions, and analysed with Compass software. In each run, each well contained antibody of interest (9101L, phospho-ERK1/2$^{T202/Y204}$; 9102L, total ERK1/2, Cell Signalling) and normalised to loading control antibody (6487S, α-actinin, Cell Signalling) in each well.

Human Phospho-Kinase Arrays (ARY003C, R&D Systems) were placed in 1.5 ml array buffer 1 and agitated gently for 1 hr at room temperature. Array buffer was substituted by dilute lysate (100 µg/ml) and left overnight at 4ºC. Membranes were subsequently washed in 3x wash buffer for 10 minutes and then incubated in detection antibody for 2 hrs at room temperature. The arrays were rinsed a further 3 times in wash buffer then covered by Streptavidin-HRP in 1X Array Buffer and incubated at room temperature for 30 minutes. They were visualised using the LI-COR Imaging System and analysed using the Quick Spots Image Analysis Software (R&D Systems). Briefly, the pixel density of each spot on the array was measured, and then the average signal of the pair of duplicate spots representing each p-RTK was calculated. Finally, the averaged background signal from each RTK spot was subtracted.

For treatment with trametinib or dasatinib, cells were incubated in complete media with vehicle (DMSO) or increasing concentrations of drug (0.01, 0.1, 1, 10 µM) and protein was collected at 30min post-treatment. Samples were lysed by using lysis buffer (CST) containing phosphatase inhibitor cocktail (Sigma, Poole, UK) and protease inhibitor cocktail (Roche Diagnostics, Burgess Hill, UK).

25

Proteomics

Cell pellets were lysed in 5% SDS/100 mM TEAB buffer with probe sonication and heating at 95ºC for 10 min, and protein concentration measured by Pierce 660 nm Protein Assay. 300 μg protein were reduced with TCEP (5 mM tris-2-carboxyethyl phosphine) and alkylated by iodoacetamide, and then purified by methanol/chloroform precipitation. Trypsin was added at 1:30 ratio (trypsin:proteins) for 18 hours digestion at 37ºC. 150 μg of peptides per sample were tandem mass tagged (TMT) labelled as instructed by the manufacturer (Thermo Scientific). The TMT labelled peptide mixture was fractionated by C18 column at pH 10, fractions were collected and pooled. Phospho-peptide enrichment used the High-Select Fe-NTA Phospho-peptide Enrichment Kit. Samples were analysed on an Orbitrap Fusion Lumos coupled with an Ultimate 3000 RSLCnano System (Thermo Scientific) using the Synchronous Precursor Selection method with dynamic exclusion enabled (as reported in PMID 28854368). All raw files were processed in Proteome Discoverer 2.3 (phospho-proteome) or 2.4 (full proteome) (Thermo Fisher) using the SequestHT search engine. Spectra were searched against reviewed Uniprot Homo sapiens entries (November 2019) and an in-house contaminate database. Search parameters for phospho-proteome were: trypsin with up to 2 miss-cleavage sites, mass tolerances at 20 ppm for Precursor, and 0.02 Da for fragment ions, dynamic modifications of Deamidated (N, Q), Oxidation (M) and Phospho (S, T, Y), and static modifications of Carbamidomethyl and TMT6plex (peptide N-terminus and K). For full proteome, fragment ion tolerance was 0.5 Da, dynamic modification of Oxidation (M) and acetylation (Protein N-terminus), and static modifications of Carbamidomethyl and TMT6plex (peptide N-terminus and K). Peptides were validated by Percolator with q-value set at 0.05. Phosphorylation site localization probabilities were computed by the ptmRS node. The TMT10plex reporter ion quantifier included 20 ppm integration tolerance on the most confident centroid peak at the MS3 level of unique peptides. Peptides with average reported S/N>3 were

26

used for protein quantification, and the SPS mass matches threshold was set at 55%. Only master proteins were reported.

Orthotopic xenograft studies

All *in vivo* experiments were approved by the local Animal Welfare and Ethics Review Board (AWERB) at the Institute of Cancer Research, and were carried out in accordance with the UK Home Office Animals (Scientific Procedures) Act 1986, the United Kingdom National Cancer Research Institute guidelines for the welfare of animals in cancer research and the ARRIVE (animal research: reporting *in vivo* experiments) guidelines (70). A single cell suspension was prepared from cells from tissue (PDX, n=9) immediately prior to implantation in in NOD.Cg-*Prkdc^{scid} Il2rg^{tm1Wjl}*/SzJ (NSG) mice (Charles River, UK). Animals were anesthetized with 4% isoflurane and maintained at 2-3% isoflurane delivered in oxygen (1 L/min). Mice were placed on a stereotactic apparatus for orthotopic implantation, with coordinates x=+1.0, z=-0.8, y=-4mm from the lambda used for delivery to the pons. 5 μL of cell suspension (250,000 cells) were stereotactically implanted per animal, using a 25-gauge SGE standard fixed needle syringe (SGE™ 005000) at a rate of rate of 1 μl/min for PDX and 2 μl/min for CDX using a digital pump (HA1100, Pico Plus Elite, Harvard Apparatus, Holliston, MA, USA). For the trametinib efficacy study, mice (29-33 days old) were randomized according to tumour volume determined by MRI into two groups: Group 1 – vehicle (10% DMSO, w/v hydroxyproylbetacyclodextrin dissolved in PBS, oral gavage (PO), q.d.) and Group 2 – trametinib (1 mg/kg, PO, q.d.). Animals were treated for 8 weeks, 5 days on, 2 days off, and treatment started at day 55 post-injection. ^{1}H MRI was performed using a horizontal bore Bruker Biospec 70/20 equipped with physiological monitoring equipment (SA Instruments) using a 2cm x 2cm mouse brain array coil. Anaesthesia was induced using 3% isoflurane delivered in oxygen (0.5l/min) and maintained at 1-2%. Core body temperature was maintained using a thermo-regulated water-heated blanket. Following optimization of the magnetic field homogeneity using a localised map shim over the whole brain, a rapid acquisition with relaxation enhancement (RARE) T_2-weighted sequence (repetition time

27

(T_R) = 4500ms, effective echo time (T_{Eeff}) = 36ms, 2 averages, RARE factor = 8, in-plane resolution 98μm x 98μm, 1mm thick contiguous slices) was used for localisation and assessment of tumours. Mice were weighed twice a week and sacrificed by cervical dislocation upon deterioration of condition and tissue taken for further analysis. For immunohistochemistry, sodium citrate (pH 6.0) heat-mediated antigen retrieval was performed and staining was carried out using antibodies directed against Human Nuclear Antigen (HNA) (1:100, Millipore, MAB4383) diluted into 1% Tris buffer solution with 0.05% Tween-20, and incubated 1 hour at room temperature. Novocastra Novolink Polymer Detection Systems Kit (Leica Biosystem, RE-7150) was used for detection. Slides were mounted using Leica CV Ultra mounting medium (Leica, 070937891).

Coronal whole brain organotypic slice

All animal procedures were under the European Communities Council Directive N. 2010/63/EU and the Italian Ministry of Health guidelines (DL 26/2014) and approved by the Italian Ministry of Health and by the local Institutional Animal Care and Use Committee (IACUC) at Istituto Superiore di Sanità (Rome, Italy; protocol n. D9997.N.BYG, 2019). Coronal whole brain organotypic slices encompassing the pons were prepared from CD1 mice pups (postnatal day 6–7) (Charles River, Wilmington, MA, USA) as previously described(71), with some modifications. In brief, mice were decapitated, and brains rapidly dissected and placed in ice-cold artificial cerebrospinal fluid (ACSF) containing (in mM): 126 NaCl, 3.5 KCl, 1.2 NaH_2PO_4, 1.2 $MgCl_2$, 2 $CaCl_2$, 25 $NaHCO_3$ and 11 glucose (pH 7.3), saturated with 95% O_2 and 5% CO_2. The brain was then embedded in 3% SeaPlaque™ agarose (Lonza, Basel, Switzerland) in PBS and 300 μm thick coronal slices were cut on a vibrating microtome (Campden Instruments, Sileby, UK), constantly cooled and oxygenated. Each slice was transferred onto a porous membrane (0.45 μm pore size, Millipore) placed on a Millipore culture insert (Millipore), inserted into six-well plates with 1.2 mL of cell culture medium/well, where the inserts were placed. The slices were incubated at 35°C, 5% CO_2 for 7 days before the experiments to allow the inflammatory reaction following the mechanical procedure to

28

subside. Following the first day of culture, the medium was replaced with fresh medium and, from that time, changed every 48h. Seven days after slices were sectioned, ICR-B169 parental neurospheres of a 250-300µm diameter (1 NS/slice) were implanted on the pontine area, and following 3 days of co-culture, preparations were treated for 4 days with 1µM dasatinib, 0.1234µM trametinib, or both, compared to vehicle control (DMSO). After this time, slices were fixed with 10% buffered formalin for 2 hour at RT and washed twice with PBS, for 10 min. Slices were then permeabilized with 1% Triton in PBS for 90 min and then blocked with 10% goat serum + 1% BSA + 0,1% Triton for 60 min. Slices were incubated O.N. with anti-human nuclei antibody (Millipore, 1:300). Slices were washed with PBS twice for 10 min and incubated with the secondary antibody (Alexa fluor-555 goat anti-mouse, Invitrogen; 1:500 O.N.). Hoechst33342 was used as a counterstain (Invitrogen, 1:10,000 in PBS for 45 min at RT). Images were taken on an Operetta CLS (PerkinElmer) in confocal mode (10X; z-stack 42 µm).

Statistical analysis

Statistical analysis was carried out using R 3.3.0 (www.r-project.org) and GraphPad Prism 8. Categorical analyses were carried out by ANOVA, with multiple comparisons subjected to Dunnett's test. In vitro dose-response effects were compared by area under the curve (AUC) analysis. Normalised and scaled abundances proteins and phospho-peptides were compared by using a Student's t-test. For these and gene expression data analysis multiple testing corrections were made using FDR according to Benjamini and Hochberg. Effects of drug treatment on survival as the primary endpoint and overall survival in the orthotopic *in vivo* models were assessed using Mantel Cox log-rank test. Adjusted P-values < 0.05 was considered significant.

Data accessibility

All newly generated sequencing data have been deposited in the European Genome-phenome Archive (ebi.ac.uk/ega) with accession number EGAS00001004495 (sequencing) or ArrayExpress (ebi.ac.uk/arrayexpress/) with accession number E-MTAB-9282 (methylation

29

arrays). Proteomic data has been deposited in the Proteomics Identifications Database (PRIDE, ebi.ac.uk/pride) with accession number PXD019701. Curated gene-level mutation, copy number, and expression data are provided as part of the pediatric-specific implementation of the cBioPortal genomic data visualisation portal (pedcbioportal.org)

30

REFERENCES

1. Avruch J, Khokhlatchev A, Kyriakis JM, Luo Z, Tzivion G, Vavvas D*, et al.* Ras activation of the Raf kinase: tyrosine kinase recruitment of the MAP kinase cascade. Recent progress in hormone research **2001**;56:127-55 doi 10.1210/rp.56.1.127.

2. Zaman A, Wu W, Bivona TG. Targeting Oncogenic BRAF: Past, Present, and Future. Cancers (Basel) **2019**;11(8):1197 doi 10.3390/cancers11081197.

3. Yao Z, Torres NM, Tao A, Gao Y, Luo L, Li Q*, et al.* BRAF Mutants Evade ERK-Dependent Feedback by Different Mechanisms that Determine Their Sensitivity to Pharmacologic Inhibition. Cancer Cell **2015**;28(3):370-83 doi 10.1016/j.ccell.2015.08.001.

4. Yao Z, Yaeger R, Rodrik-Outmezguine VS, Tao A, Torres NM, Chang MT*, et al.* Tumours with class 3 BRAF mutants are sensitive to the inhibition of activated RAS. Nature **2017**;548(7666):234-8 doi 10.1038/nature23291.

5. Truong AY, Nicolaides TP. Targeted Therapy for MAPK Alterations in Pediatric Gliomas. Brain Disord Ther **2015**;Suppl 2:005 doi 10.4172/2168-975X.S2-005.

6. Jones DT, Kocialkowski S, Liu L, Pearson DM, Backlund LM, Ichimura K*, et al.* Tandem duplication producing a novel oncogenic BRAF fusion gene defines the majority of pilocytic astrocytomas. Cancer research **2008**;68(21):8673-7 doi 10.1158/0008-5472.CAN-08-2097.

7. Zhang J, Wu G, Miller CP, Tatevossian RG, Dalton JD, Tang B*, et al.* Whole-genome sequencing identifies genetic alterations in pediatric low-grade gliomas. Nature genetics **2013**;45(6):602-12 doi 10.1038/ng.2611.

8. Rivera B, Gayden T, Carrot-Zhang J, Nadaf J, Boshari T, Faury D*, et al.* Germline and somatic FGFR1 abnormalities in dysembryoplastic neuroepithelial tumors. Acta Neuropathol **2016**;131(6):847-63 doi 10.1007/s00401-016-1549-x.

9. Stone TJ, Keeley A, Virasami A, Harkness W, Tisdall M, Izquierdo Delgado E*, et al.* Comprehensive molecular characterisation of epilepsy-associated glioneuronal tumours. Acta Neuropathol **2018**;135(1):115-29 doi 10.1007/s00401-017-1773-z.

10. Qaddoumi I, Orisme W, Wen J, Santiago T, Gupta K, Dalton JD*, et al.* Genetic alterations in uncommon low-grade neuroepithelial tumors: BRAF, FGFR1, and MYB mutations occur at high frequency and align with morphology. Acta Neuropathol **2016**;131(6):833-45 doi 10.1007/s00401-016-1539-z.

11. Lassaletta A, Zapotocky M, Mistry M, Ramaswamy V, Honnorat M, Krishnatry R*, et al.* Therapeutic and Prognostic Implications of BRAF V600E in Pediatric Low-Grade Gliomas. Journal of clinical oncology : official journal of the American Society of Clinical Oncology **2017**;35(25):2934-41 doi 10.1200/jco.2016.71.8726.

12. Schindler G, Capper D, Meyer J, Janzarik W, Omran H, Herold-Mende C*, et al.* Analysis of BRAF V600E mutation in 1,320 nervous system tumors reveals high mutation frequencies in pleomorphic xanthoastrocytoma, ganglioglioma and extra-cerebellar pilocytic astrocytoma. Acta Neuropathol **2011**;121(3):397-405 doi 10.1007/s00401-011-0802-6.

13. Mackay A, Burford A, Carvalho D, Izquierdo E, Fazal-Salom J, Taylor KR*, et al.* Integrated Molecular Meta-Analysis of 1,000 Pediatric High-Grade and Diffuse Intrinsic Pontine Glioma. Cancer Cell **2017**; 32(4):520-537 doi 10.1016/j.ccell.2017.08.017.

14.   Guerreiro Stucklin AS, Ryall S, Fukuoka K, Zapotocky M, Lassaletta A, Li C, *et al.* Alterations in ALK/ROS1/NTRK/MET drive a group of infantile hemispheric gliomas. Nature communications **2019**;10(1):4343 doi 10.1038/s41467-019-12187-5.

15.   Clarke M, Mackay A, Ismer B, Pickles JC, Tatevossian RG, Newman S, *et al.* Infant high grade gliomas comprise multiple subgroups characterized by novel targetable gene fusions and favorable outcomes. Cancer discovery **2020**; 10(7):942-963 doi 10.1158/2159-8290.Cd-19-1030.

16.   Mackay A, Burford A, Molinari V, Jones DTW, Izquierdo E, Brouwer-Visser J, *et al.* Molecular, Pathological, Radiological, and Immune Profiling of Non-brainstem Pediatric High-Grade Glioma from the HERBY Phase II Randomized Trial. Cancer Cell **2018**;33(5):829-42 e5 doi 10.1016/j.ccell.2018.04.004.

17.   Bender S, Gronych J, Warnatz H-J, Hutter B, Gröbner S, Ryzhova M, *et al.* Recurrent MET fusion genes represent a drug target in pediatric glioblastoma. Nature medicine **2016**;22(11):1314-20 doi 10.1038/nm.4204.

18.   Mistry M, Zhukova N, Merico D, Rakopoulos P, Krishnatry R, Shago M, *et al.* BRAF mutation and CDKN2A deletion define a clinically distinct subgroup of childhood secondary high-grade glioma. J Clin Oncol **2015**;33(9):1015-22 doi 10.1200/JCO.2014.58.3922.

19.   Wu G, Diaz AK, Paugh BS, Rankin SL, Ju B, Li Y, *et al.* The genomic landscape of diffuse intrinsic pontine glioma and pediatric non-brainstem high-grade glioma. Nature genetics **2014**;46(5):444-50 doi 10.1038/ng.2938.

20.   Jones C, Perryman L, Hargrave D. Paediatric and adult malignant glioma: close relatives or distant cousins? Nat Rev Clin Oncol **2012**;9(7):400-13 doi 10.1038/nrclinonc.2012.87.

21.   Jones C, Karajannis MA, Jones DTW, Kieran MW, Monje M, Baker SJ, *et al.* Pediatric high-grade glioma: biologically and clinically in need of new thinking. Neuro-oncology **2017**;19(2):153-61 doi 10.1093/neuonc/now101.

22.   McGranahan N, Swanton C. Biological and therapeutic impact of intratumor heterogeneity in cancer evolution. Cancer Cell **2015**;27(1):15-26 doi 10.1016/j.ccell.2014.12.001.

23.   Hata AN, Niederst MJ, Archibald HL, Gomez-Caraballo M, Siddiqui FM, Mulvey HE, *et al.* Tumor cells can follow distinct evolutionary paths to become resistant to epidermal growth factor receptor inhibition. Nature medicine **2016**;22(3):262-9 doi 10.1038/nm.4040.

24.   Shi H, Hugo W, Kong X, Hong A, Koya RC, Moriceau G, *et al.* Acquired resistance and clonal evolution in melanoma during BRAF inhibitor therapy. Cancer discovery **2014**;4(1):80-93 doi 10.1158/2159-8290.Cd-13-0642.

25.   Bhang HE, Ruddy DA, Krishnamurthy Radhakrishna V, Caushi JX, Zhao R, Hims MM, *et al.* Studying clonal dynamics in response to cancer therapy using high-complexity barcoding. Nature medicine **2015**;21(5):440-8 doi 10.1038/nm.3841.

26.   Turke AB, Zejnullahu K, Wu Y-L, Song Y, Dias-Santagata D, Lifshits E, *et al.* Preexistence and clonal selection of MET amplification in EGFR mutant NSCLC. Cancer Cell **2010**;17(1):77-88 doi 10.1016/j.ccr.2009.11.022.

27.   Ramirez M, Rajaram S, Steininger RJ, Osipchuk D, Roth MA, Morinishi LS, *et al.* Diverse drug-resistance mechanisms can emerge from drug-tolerant cancer persister cells. Nature communications **2016**;7(1):10690 doi 10.1038/ncomms10690.

28.   Chapman PB, Hauschild A, Robert C, Haanen JB, Ascierto P, Larkin J, *et al.* Improved survival with vemurafenib in melanoma with BRAF V600E mutation. N Engl J Med **2011**;364(26):2507-16 doi 10.1056/NEJMoa1103782.

29.   Flaherty KT, Puzanov I, Kim KB, Ribas A, McArthur GA, Sosman JA, *et al.* Inhibition of mutated, activated BRAF in metastatic melanoma. N Engl J Med **2010**;363(9):809-19 doi 10.1056/NEJMoa1002011.

30.   Flaherty KT, Robert C, Hersey P, Nathan P, Garbe C, Milhem M, *et al.* Improved survival with MEK inhibition in BRAF-mutated melanoma. N Engl J Med **2012**;367(2):107-14 doi 10.1056/NEJMoa1203421.

31.   Emery CM, Vijayendran KG, Zipser MC, Sawyer AM, Niu L, Kim JJ, *et al.* MEK1 mutations confer resistance to MEK and B-RAF inhibition. Proceedings of the National Academy of Sciences **2009**;106(48):20411 doi 10.1073/pnas.0905833106.

32.   Wagle N, Emery C, Berger MF, Davis MJ, Sawyer A, Pochanard P, *et al.* Dissecting therapeutic resistance to RAF inhibition in melanoma by tumor genomic profiling. Journal of clinical oncology : official journal of the American Society of Clinical Oncology **2011**;29(22):3085-96 doi 10.1200/jco.2010.33.2312.

33.   Rizos H, Menzies AM, Pupo GM, Carlino MS, Fung C, Hyman J, *et al.* BRAF inhibitor resistance mechanisms in metastatic melanoma: spectrum and clinical impact. Clinical cancer research : an official journal of the American Association for Cancer Research **2014**;20(7):1965-77 doi 10.1158/1078-0432.Ccr-13-3122.

34.   Johnson DB, Menzies AM, Zimmer L, Eroglu Z, Ye F, Zhao S, *et al.* Acquired BRAF inhibitor resistance: A multicenter meta-analysis of the spectrum and frequencies, clinical behaviour, and phenotypic associations of resistance mechanisms. European journal of cancer (Oxford, England : 1990) **2015**;51(18):2792-9 doi 10.1016/j.ejca.2015.08.022.

35.   Flaherty KT, Infante JR, Daud A, Gonzalez R, Kefford RF, Sosman J, *et al.* Combined BRAF and MEK inhibition in melanoma with BRAF V600 mutations. N Engl J Med **2012**;367(18):1694-703 doi 10.1056/NEJMoa1210093.

36.   Long GV, Stroyakovskiy D, Gogas H, Levchenko E, de Braud F, Larkin J, *et al.* Combined BRAF and MEK inhibition versus BRAF inhibition alone in melanoma. N Engl J Med **2014**;371(20):1877-88 doi 10.1056/NEJMoa1406037.

37.   Villanueva J, Infante JR, Krepler C, Reyes-Uribe P, Samanta M, Chen HY, *et al.* Concurrent MEK2 mutation and BRAF amplification confer resistance to BRAF and MEK inhibitors in melanoma. Cell reports **2013**;4(6):1090-9 doi 10.1016/j.celrep.2013.08.023.

38.   Long GV, Fung C, Menzies AM, Pupo GM, Carlino MS, Hyman J, *et al.* Increased MAPK reactivation in early resistance to dabrafenib/trametinib combination therapy of BRAF-mutant metastatic melanoma. Nature communications **2014**;5(1):5694 doi 10.1038/ncomms6694.

39.   Wagle N, Van Allen EM, Treacy DJ, Frederick DT, Cooper ZA, Taylor-Weiner A, *et al.* MAP kinase pathway alterations in BRAF-mutant melanoma patients with acquired resistance to combined RAF/MEK inhibition. Cancer discovery **2014**;4(1):61-8 doi 10.1158/2159-8290.Cd-13-0631.

40.   Moriceau G, Hugo W, Hong A, Shi H, Kong X, Yu CC, *et al.* Tunable-combinatorial mechanisms of acquired resistance limit the efficacy of BRAF/MEK cotargeting but result in melanoma drug addiction. Cancer Cell **2015**;27(2):240-56 doi 10.1016/j.ccell.2014.11.018.

41.   Hargrave DR, Bouffet E, Tabori U, Broniscer A, Cohen KJ, Hansford JR, *et al.* Efficacy and Safety of Dabrafenib in Pediatric Patients with BRAF V600 Mutation-Positive Relapsed or Refractory Low-Grade Glioma: Results from a Phase I/IIa Study. Clin Cancer Res **2019**;25(24):7303-11 doi 10.1158/1078-0432.CCR-19-2177.

42.   Kieran MW, Geoerger B, Dunkel IJ, Broniscer A, Hargrave D, Hingorani P, *et al.* A Phase I and Pharmacokinetic Study of Oral Dabrafenib in Children and Adolescent Patients with Recurrent

or Refractory BRAF V600 Mutation-Positive Solid Tumors. Clin Cancer Res **2019**;25(24):7294-302 doi 10.1158/1078-0432.CCR-17-3572.

43. Castel D, Kergrohen T, Tauziède-Espariat A, Mackay A, Ghermaoui S, Lechapt E*, et al.* Histone H3 wild-type DIPG/DMG overexpressing EZHIP extend the spectrum diffuse midline gliomas with PRC2 inhibition beyond H3-K27M mutation. Acta Neuropathol **2020**; 139(6):1109-1113 doi 10.1007/s00401-020-02142-w.

44. Germann UA, Furey BF, Markland W, Hoover RR, Aronov AM, Roix JJ*, et al.* Targeting the MAPK Signaling Pathway in Cancer: Promising Preclinical Activity with the Novel Selective ERK1/2 Inhibitor BVD-523 (Ulixertinib). Molecular cancer therapeutics **2017**;16(11):2351-63 doi 10.1158/1535-7163.Mct-17-0456.

45. Emery CM, Monaco KA, Wang P, Balak M, Freeman A, Meltzer J*, et al.* BRAF-inhibitor Associated MEK Mutations Increase RAF-Dependent and -Independent Enzymatic Activity. Molecular cancer research : MCR **2017**;15(10):1431-44 doi 10.1158/1541-7786.Mcr-17-0211.

46. Perreault S, Larouche V, Tabori U, Hawkin C, Lippe S, Ellezam B*, et al.* A phase 2 study of trametinib for patients with pediatric glioma or plexiform neurofibroma with refractory tumor and activation of the MAPK/ERK pathway: TRAM-01. BMC cancer **2019**;19(1):1250 doi 10.1186/s12885-019-6442-2.

47. Jaiswal BS, Janakiraman V, Kljavin NM, Chaudhuri S, Stern HM, Wang W*, et al.* Somatic mutations in p85alpha promote tumorigenesis through class IA PI3K activation. Cancer Cell **2009**;16(6):463-74 doi 10.1016/j.ccr.2009.10.016.

48. Jubb HC, Saini HK, Verdonk ML, Forbes SA. COSMIC-3D provides structural perspectives on cancer genetics for drug discovery. Nat Genet **2018**;50(9):1200-2 doi 10.1038/s41588-018-0214-9.

49. Ross RL, Burns JE, Taylor CF, Mellor P, Anderson DH, Knowles MA. Identification of mutations in distinct regions of p85 alpha in urothelial cancer. PLoS One **2013**;8(12):e84411-e doi 10.1371/journal.pone.0084411.

50. Cheung LW, Yu S, Zhang D, Li J, Ng PK, Panupinthu N*, et al.* Naturally occurring neomorphic PIK3R1 mutations activate the MAPK pathway, dictating therapeutic response to MAPK pathway inhibitors. Cancer Cell **2014**;26(4):479-94 doi 10.1016/j.ccell.2014.08.017.

51. Brinckmann A, Mischung C, Bassmann I, Kuhnisch J, Schuelke M, Tinschert S*, et al.* Detection of novel NF1 mutations and rapid mutation prescreening with Pyrosequencing. Electrophoresis **2007**;28(23):4295-301 doi 10.1002/elps.200700118.

52. See WL, Tan IL, Mukherjee J, Nicolaides T, Pieper RO. Sensitivity of glioblastomas to clinically available MEK inhibitors is defined by neurofibromin 1 deficiency. Cancer research **2012**;72(13):3350-9 doi 10.1158/0008-5472.Can-12-0334.

53. Ameratunga M, McArthur G, Gan H, Cher L. Prolonged disease control with MEK inhibitor in neurofibromatosis type I-associated glioblastoma. Journal of clinical pharmacy and therapeutics **2016**;41(3):357-9 doi 10.1111/jcpt.12378.

54. Romo CG, Slobogean BL, Blair LK, Blakeley JON. Trametinib for aggressive gliomas in adults with neurofibromatosis type 1. Journal of Clinical Oncology **2019**;37(15_suppl):e13562-e doi 10.1200/JCO.2019.37.15_suppl.e13562.

55. Fangusaro J, Onar-Thomas A, Young Poussaint T, Wu S, Ligon AH, Lindeman N*, et al.* Selumetinib in paediatric patients with BRAF-aberrant or neurofibromatosis type 1-associated recurrent, refractory, or progressive low-grade glioma: a multicentre, phase 2 trial. The Lancet Oncology **2019**;20(7):1011-22 doi 10.1016/s1470-2045(19)30277-3.

56.   Noeparast A, Teugels E, Giron P, Verschelden G, De Brakeleer S, Decoster L*, et al.* Non-V600 BRAF mutations recurrently found in lung cancer predict sensitivity to the combination of Trametinib and Dabrafenib. Oncotarget **2017**;8(36):60094-108 doi 10.18632/oncotarget.11635.

57.   Wu P-K, Park J-I. MEK1/2 Inhibitors: Molecular Activity and Resistance Mechanisms. Seminars in Oncology **2015**;42(6):849-62 doi https://doi.org/10.1053/j.seminoncol.2015.09.023.

58.   Gao Y, Chang MT, McKay D, Na N, Zhou B, Yaeger R*, et al.* Allele-Specific Mechanisms of Activation of MEK1 Mutants Determine Their Properties. Cancer Discov **2018**;8(5):648-61 doi 10.1158/2159-8290.CD-17-1452.

59.   Catalanotti F, Solit DB, Pulitzer MP, Berger MF, Scott SN, Iyriboz T*, et al.* Phase II trial of MEK inhibitor selumetinib (AZD6244, ARRY-142886) in patients with BRAFV600E/K-mutated melanoma. Clinical cancer research : an official journal of the American Association for Cancer Research **2013**;19(8):2257-64 doi 10.1158/1078-0432.CCR-12-3476.

60.   Kalluri R, Weinberg RA. The basics of epithelial-mesenchymal transition. The Journal of clinical investigation **2009**;119(6):1420-8 doi 10.1172/jci39104.

61.   Fedele M, Cerchia L, Pegoraro S, Sgarra R, Manfioletti G. Proneural-Mesenchymal Transition: Phenotypic Plasticity to Acquire Multitherapy Resistance in Glioblastoma. Int J Mol Sci **2019**;20(11):2746 doi 10.3390/ijms20112746.

62.   Segerman A, Niklasson M, Haglund C, Bergstrom T, Jarvius M, Xie Y*, et al.* Clonal Variation in Drug and Radiation Response among Glioma-Initiating Cells Is Linked to Proneural-Mesenchymal Transition. Cell reports **2016**;17(11):2994-3009 doi 10.1016/j.celrep.2016.11.056.

63.   Jing J, Greshock J, Holbrook JD, Gilmartin A, Zhang X, McNeil E*, et al.* Comprehensive predictive biomarker analysis for MEK inhibitor GSK1120212. Molecular cancer therapeutics **2012**;11(3):720-9 doi 10.1158/1535-7163.Mct-11-0505.

64.   Wilson C, Nicholes K, Bustos D, Lin E, Song Q, Stephan JP*, et al.* Overcoming EMT-associated resistance to anti-cancer drugs via Src/FAK pathway inhibition. Oncotarget **2014**;5(17):7328-41 doi 10.18632/oncotarget.2397.

65.   Rao G, Kim IK, Conforti F, Liu J, Zhang YW, Giaccone G. Dasatinib sensitises KRAS-mutant cancer cells to mitogen-activated protein kinase kinase inhibitor via inhibition of TAZ activity. European journal of cancer (Oxford, England : 1990) **2018**;99:37-48 doi 10.1016/j.ejca.2018.05.013.

66.   Acar A, Nichol D, Fernandez-Mateos J, Cresswell GD, Barozzi I, Hong SP*, et al.* Exploiting evolutionary steering to induce collateral drug sensitivity in cancer. Nature communications **2020**;11(1):1923 doi 10.1038/s41467-020-15596-z.

67.   Capper D, Jones DTW, Sill M, Hovestadt V, Schrimpf D, Sturm D*, et al.* DNA methylation-based classification of central nervous system tumours. Nature **2018**;555(7697):469-74 doi 10.1038/nature26000.

68.   Ianevski A, Giri AK, Aittokallio T. SynergyFinder 2.0: visual analytics of multi-drug combination synergies. Nucleic Acids Res **2020** doi 10.1093/nar/gkaa216.

69.   Ianevski A, He L, Aittokallio T, Tang J. SynergyFinder: a web application for analyzing drug combination dose-response matrix data. Bioinformatics (Oxford, England) **2017**;33(15):2413-5 doi 10.1093/bioinformatics/btx162.

70.   Kilkenny C, Browne WJ, Cuthill IC, Emerson M, Altman DG. Improving bioscience research reporting: the ARRIVE guidelines for reporting animal research. PLoS Biol **2010**;8(6):e1000412 doi 10.1371/journal.pbio.1000412.

71.   Pericoli G, Petrini S, Giorda E, Ferretti R, Ajmone-Cat MA, Court W, *et al.* Integration of Multiple
       Platforms for the Analysis of Multifluorescent Marking Technology Applied to Pediatric GBM
       and DIPG. Int J Mol Sci **2020**;21(18) doi 10.3390/ijms21186763.

FIGURE LEGENDS

Figure 1 - *In vitro sensitivity to trametinib in patient-derived DIPG models.* (A) Oncoprint representation of an integrated annotation of single nucleotide variants, DNA copy number changes and structural variants for patient-derived models and tumour biopsy specimens. Samples are arranged in columns with genes labelled along rows. Clinicopathological and molecular annotations are provided as bars according to the included key. (B) t-statistic based stochastic neighbor embedding (t-SNE) projection of a combined methylation dataset comprising the *in vitro* models (circled) plus a reference set of glioma subtypes (n=1766). The first two projections are plotted on the x and y axes, with samples represented by dots colored by subtype as labelled on the figure. (C) Drug sensitivities in the mini-screens carried out on cells grown under 2D and 3D conditions, visualised by heatmap of normalised area under the curve values (AUC). Clinicopathological and molecular annotations are provided as bars according to the included key. (D) Dose-response curves for the MEK inhibitor trametinib tested against patient-derived models *in vitro* grown in 2D; (E) Dose-response curves for the MEK inhibitor trametinib tested against patient-derived models *in vitro* grown in 3D. Cells harbouring MAPK pathway alterations highlighted in blue. Concentration of compound is plotted on a log scale (x axis) against cell viability (y axis). Mean plus standard error are plotted from at least n=3 experiments.

Figure 2 – *PIK3R1 and NF1 mutations drive the sensitivity of DIPG cells to trametinib.* (A) Cartoon representing the protein domains of PIK3R1 showing the mutant residue for the observed hotspot N564D mutation observed in ICR-B181. (B) Cartoon representing the protein domains of NF1 showing the mutant residue for the observed I1824S missense mutation observed in ICR-B184. Generated in ProteinPaint (pecan.stjude.cloud/proteinpaint). (C) Dose-response validation curves for trametinib tested against ICR-B181 cells *in vitro* grown in 3D (*PIK3R1*_N564D, blue) and 2D (*PIK3R1* wild-type, grey). (D) Dose-response

curves for trametinib tested against ICR-B184 cells *in vitro* grown in 3D (*NF1*_I1824S, blue) and 2D (*NF1* wild-type, grey). Concentration of compound is plotted on a log scale (x axis) against cell viability (y axis). Mean plus standard error are plotted from at least n=3 experiments. ****p<0.0001, AUC t-test. (E) Barplot of quantitative capillary phospho-protein assessment of phospho-ERK1/2$^{T202/Y204}$, plotted as a ratio to total ERK1/2, and normalised to the 2D (MAPK wild-type) model in each case. (F) Variant allele frequency (VAF, y axis) of PIK3R1-N564D in ICR-B181 cells grown in 3D (blue) and 2D (grey) over time, as measured by ddPCR. Passage number of cells assessed is given on the x axis. (G) Survival curves for ICR-B181-CDX models, separated by mice implanted with cells grown as either 2D (grey) or 3D (blue). (H) Anti-human nuclear antibody (HNA), staining for ICR-B181-CDX derived from cells grown in 3D, with extensive tumour cell infiltration. Sagittal sections, counterstained with haematoxylin. (I) sagittal T_2-weighted image (day 246 post-implantation) for ICR-B181-CDX derived from cells grown in 3D, showing hyperintense tumour throughout the cerebellum and upper pons (indicated by arrow). (J) Haematoxylin and eosin stained section of ICR-B181-3D CDX, showing histology consistent with high grade glioma. Scale bar is 200μm.

Figure 3 - *MEK1/2 mutations drive resistance to trametinib in BRAF_G469V-driven DIPG cells.* (A) Protein structure representation of BRAF showing the mutant residue (shaded orange) for the observed G469 missense mutation observed in ICR-B169. Generated in COSMIC-3D (cancer.sanger.ac.uk/cosmic3d). (B) Timeline of clinical experience for the child with *BRAF*_G469V mutant DIPG treated with trametinib at progression. Initial therapy with everolimus and radiotherapy is shaded in orange, later treatment with trametinib in blue. Sagittal T1-weighted post-gadolinium MRI images are provided at diagnosis, the initial progression, and the later progression immediately prior to death from disease. Periods of steroid treatment are noted by purple lines. The tumour is highlighted with arrows. (C) Survival curves for mice bearing ICR-B169 cell-derived orthotopic xenografts, treated with trametinib (blue), compared with vehicle-treated controls (grey). Treatment window is shaded in grey.

(D) Experimental design for the generation of cells resistant to trametinib by the continuous exposure model. Parental ICR-B169 cells are treated with either exponentially increasing dose of inhibitor over time (Approach 1) or by a constant IC_{80} dose (Approach 2). (E) Dose-response curves for trametinib tested against ICR-B169 parental cells (grey) and resistant clones T1 (*MEK2*_I115N, pink), (T3 *MEK1*_I141S, purple) and T6 (*MEK1*_K57N, red) after 7-9 months exposure to inhibitor. (F) Dose-response curves for trametinib tested against ICR-B169 parental cells (grey) and resistant clones (dashed lines) after 2 months withdrawal of inhibitor. Concentration of compound is plotted on a log scale (x axis) against cell viability (y axis). Mean plus standard error are plotted from at least n=3 experiments. ***p<0.001, **p<0.001, AUC t-test. (G) Emergence of *MEK1/2* mutations in clones T1 (pink), T3 (purple) and T6 (red) over time, as assessed by ddPCR. X axes represent passage number; left y axes are specific mutation variant allele frequencies (VAF); right y axes plot the concentration of trametinib cells were exposed to (grey dashed line). (H) Emergence of resistance in clones over time (T1, pink; T3, purple; T6, red), plotted as days exposed to inhibitor on the x axis, with passage numbers labelled. Y axis is GI_{50} value for trametinib in cells harvested at the given passage. (I) Pathway activation in resistant clones (T1, pink; T3, purple; T6, red) assessed by a capillary electrophoresis assay, and plotted as a ratio of respective phosphorylated/total protein compared to ICR-B169 parental cells (grey).

Figure 4 – *Integrated gene and protein expression profiling of trametinib-resistant DIPG cells.* (A) Co-ordinately down-regulated genes (left), proteins (middle) and phospho-sites (right) in all three trametinib-resistant subclones of ICR-B169 *BRAF*_G469V cells, as compared to parental. (B) Co-ordinately up-regulated genes (left), proteins (middle) and phospho-sites (right) in all three trametinib-resistant subclones, as compared to ICR-B169 parental (grey). T1 *MEK2*_I115N, pink; T3 *MEK1*_I141S, purple; T6, *MEK1*_K57N, red. (C) Gene set enrichment analysis (GSEA) enrichment plots for the signature VERHAAK_GLIOBLASTOMA_PRONEURAL in T6 *MEK1*_K57N cells compared to ICR-B169

parental. The curves show the enrichment score on the y axis and the rank list metric on the x axis. Alongside is a heatmap representation of expression of significantly differentially expressed genes in the signature in all three trametinib-resistant clones compared to parental. (D) GSEA enrichment plots for the signature HALLMARK_EPITHELIAL_MESENCHYMAL_ TRANSITION in T6 *MEK1*_K57N cells compared to ICR-B169 parental. The curves show the enrichment score on the y axis and the rank list metric on the x axis. Alongside is a heatmap representation of expression of significantly differentially expressed genes in the signature in all three trametinib-resistant clones compared to parental. (E) GSEA enrichment plots for the signature HUANG_DASATINIB_RESISTANCE_UP in T6 *MEK1*_K57N cells compared to ICR-B169 parental. The curves show the enrichment score on the y axis and the rank list metric on the x axis. Alongside is a heatmap representation of expression of significantly differentially expressed genes in the signature in all three trametinib-resistant clones compared to parental. T1 *MEK2*_I115N, pink; T3 *MEK1*_I141S, purple; T6, *MEK1*_K57N, red.

Figure 5 – *Reciprocity of drug sensitivities and gene expression signatures between trametinib and dasatinib in DIPG cells.* (A) Dose-response curves for ulixertinib tested against ICR-B169 parental cells (grey) and resistant clones T1 (*MEK2*_I115N, pink), (T3 *MEK1*_I141S, purple) and T6 (*MEK1*_K57N, red). (B) Dose-response curves for dasatinib tested against ICR-B169 parental cells (grey) and resistant clones. Concentration of compound is plotted on a log scale (x axis) against cell viability (y axis). Mean plus standard error are plotted from at least n=3 experiments. ***$p<0.001$, **$p<0.01$, *$p<0.05$, AUC t-test. (C) Boxplot of dasatinib GI_{50} values (log scale, y axis) for primary patient-derived cultures separated by trametinib sensitivity status. (D) Boxplot of trametinib GI_{50} values (log scale, y axis) for primary patient-derived cultures separated by dasatinib sensitivity status. ** $p<0.001$, t-test. (E) Gene set enrichment analysis (GSEA) enrichment plots for the signature VERHAAK_GLIOBLASTOMA_PRONEURAL in primary patient-derived cultures separated by trametinib (top) or dasatinib (bottom) sensitivity status. The curves show the enrichment score

40

on the y axis and the rank list metric on the x axis. Alongside are heatmap representations of expression of significantly differentially expressed genes in the signature in all trametinib or dasatinib resistant versus sensitive cell cultures. (F) Gene set enrichment analysis (GSEA) enrichment plots for the signature HALLMARK_EPITHELIAL_ MESENCHYMAL_TRANSITION in primary patient-derived cultures separated by trametinib (top) or dasatinib (bottom) sensitivity status. The curves show the enrichment score on the y axis and the rank list metric on the x axis. Alongside are heatmap representations of expression of significantly differentially expressed genes in the signature in all trametinib or dasatinib resistant versus sensitive cell cultures. (G) Gene set enrichment analysis (GSEA) enrichment plots for the signature HUANG_DASATINIB_RESISTANCE_UP in primary patient-derived cultures separated by trametinib (top) or dasatinib (bottom) sensitivity status. The curves show the enrichment score on the y axis and the rank list metric on the x axis. Alongside are heatmap representations of expression of significantly differentially expressed genes in the signature in all trametinib or dasatinib resistant versus sensitive cell cultures.

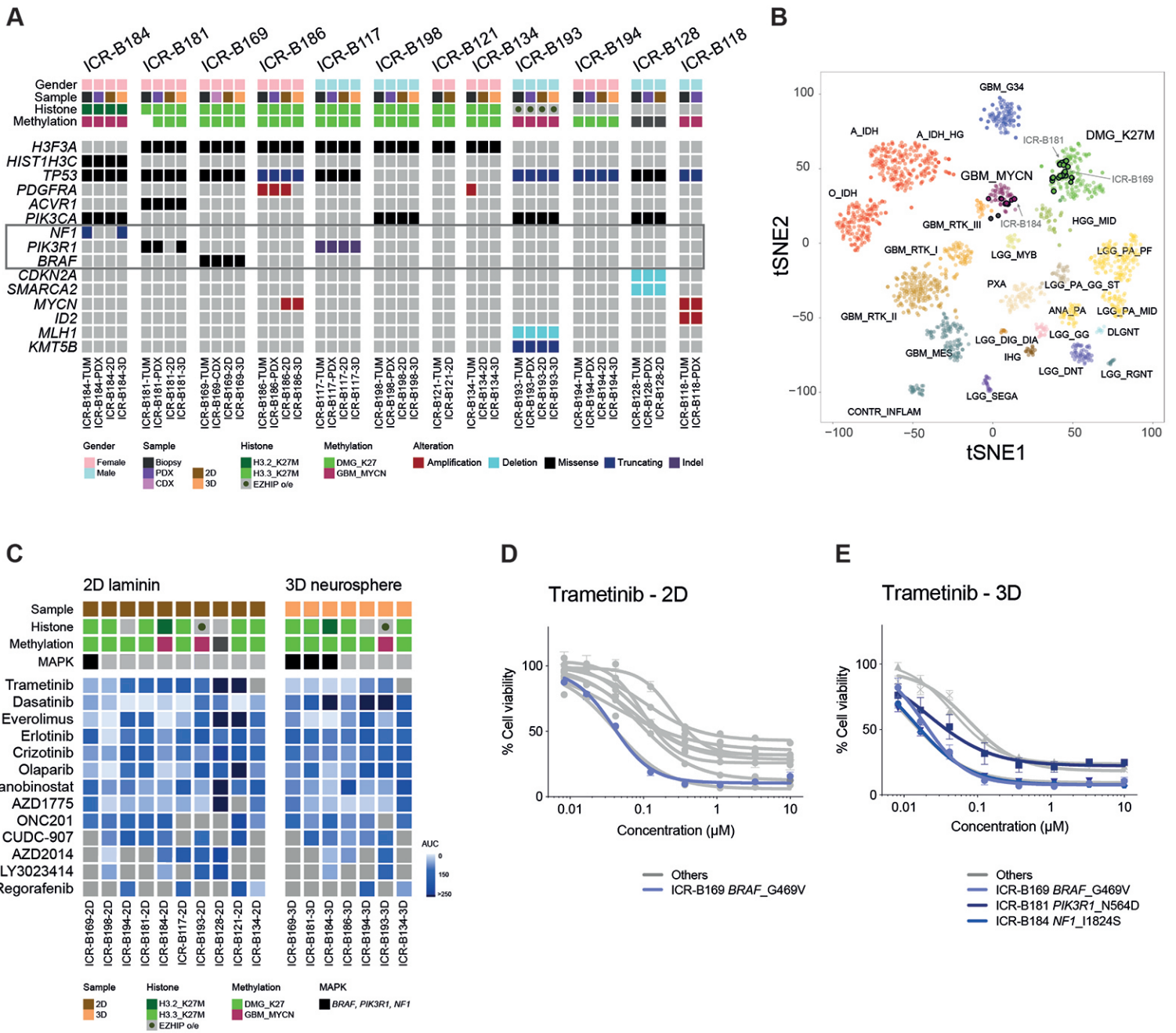**Figure 6** – *Synergy of combined dasatinib and trametinib in BRAF_G469V-driven DIPG cells.* (A) Cell viability matrices for ICR-B169 parental (grey) and trametinib-resistant clones T1 (*MEK2*_I115N, pink), (T3 *MEK1*_I141S, purple) and T6 (*MEK1*_K57N, red), treated with distinct combinations of dasatinib (y axes) and trametinib (x axes) ranging from 0-10 µM. A heatmap is overlaid to the proportions of viable cells remaining, coloured according to the key provided from 1.0 (black, all cells) to 0 (red, no viable cells). (B) Excess above BLISS matrices for ICR-B169 parental and trametinib-resistant clones treated with distinct combinations of dasatinib (y axes) and trametinib (x axes) ranging from 0-10 µM. A heatmap is overlaid to the excess score, coloured according to the key provided from 0.4 (red, enhanced effects) to 0 (green, no difference). (C) BLISS synergy maps for ICR-B169 parental and trametinib-resistant clones treated with distinct combinations of dasatinib (y axes) and trametinib (x axes)

41

ranging from 0-10 μM. The heatmap represents the δ score coloured according to the key provided from 30 (red, high degree of synergy) to -30 (green, antagonism).
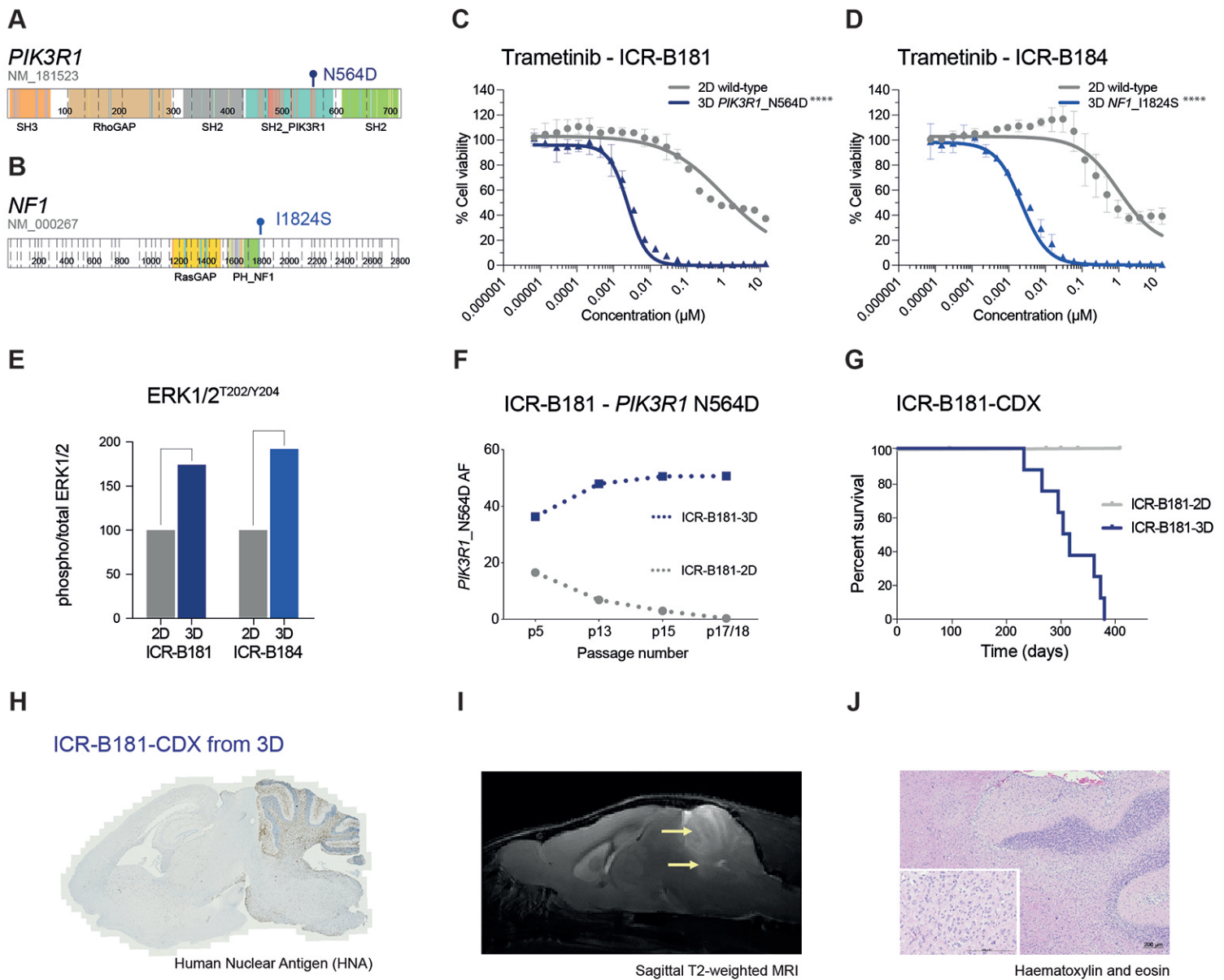
Figure 7 – *Efficacy of combined dasatinib and trametinib on ex vivo brain slice preparations.* (A) Coronal slices of normal mouse brain, counterstained with Hoechst33342 (aqua) are implanted in the pontine region with ICR-B169 parental cells, stained with human nuclear antigen (orange), and treated for 4 days with 1μM dasatinib, 0.1234μM trametinib, or both, compared to vehicle control. Scale bar is 2 mm. (B) Barplot of quantification of tumour cell infiltration across the brain parenchymal tissue as measured by the calculated area invaded compared to vehicle control. Plotted is the mean of at least 6 independent slices, error bars represent the standard deviation. ****$p<0.0001$, ***$p<0.001$, **$p<0.01$, *$p<0.05$, FDR-corrected t-test.

Figure 1

Figure 2
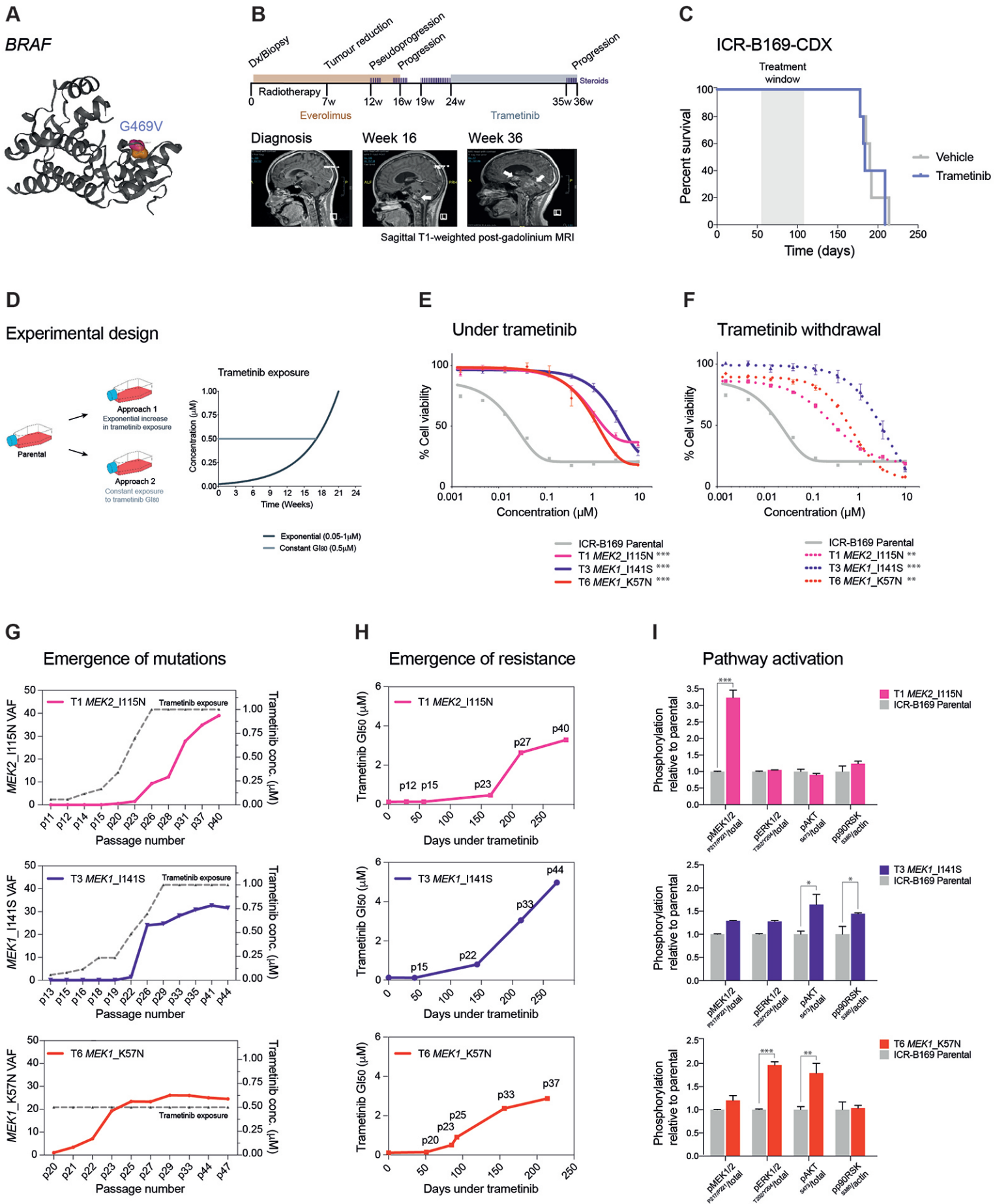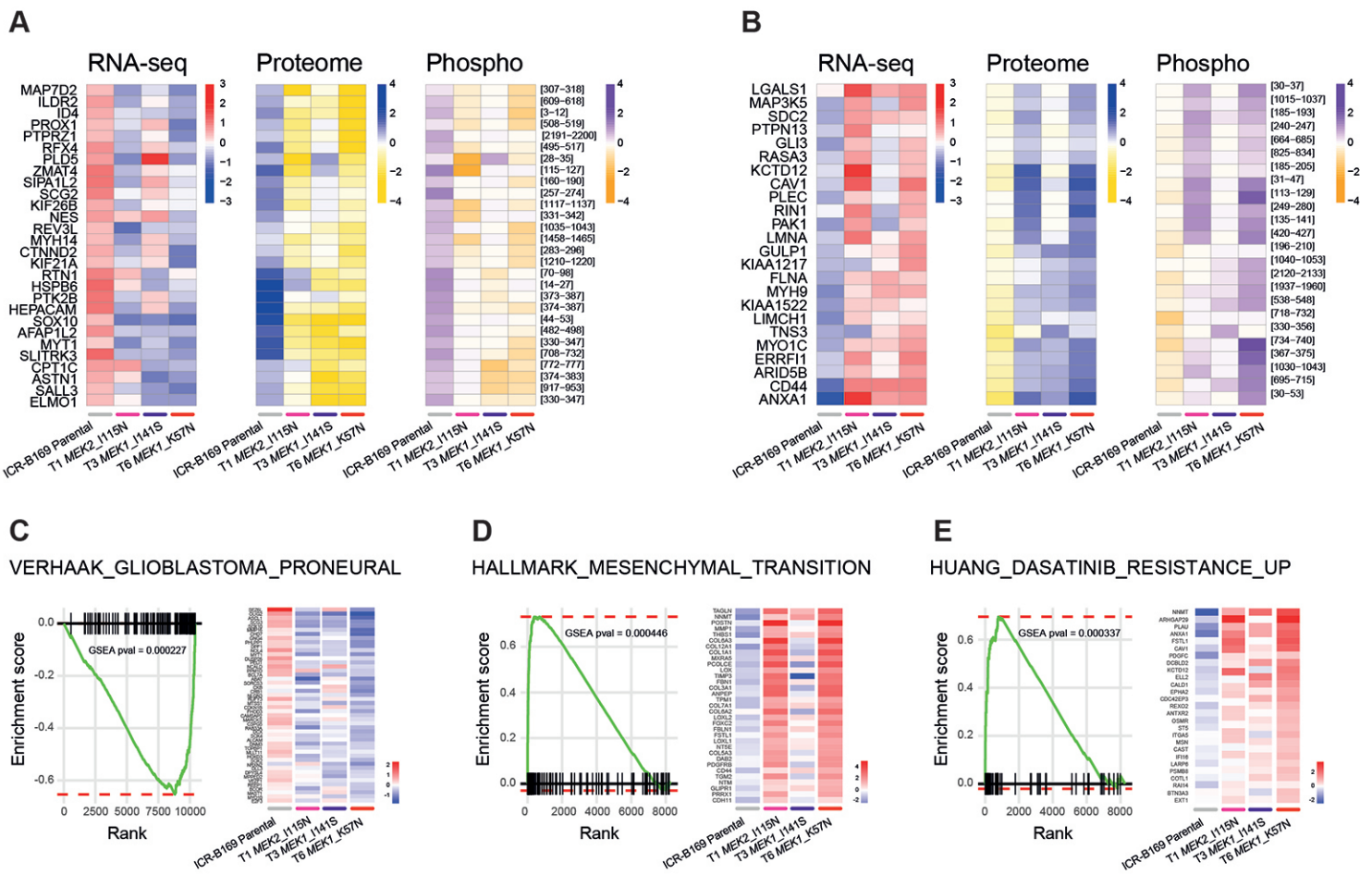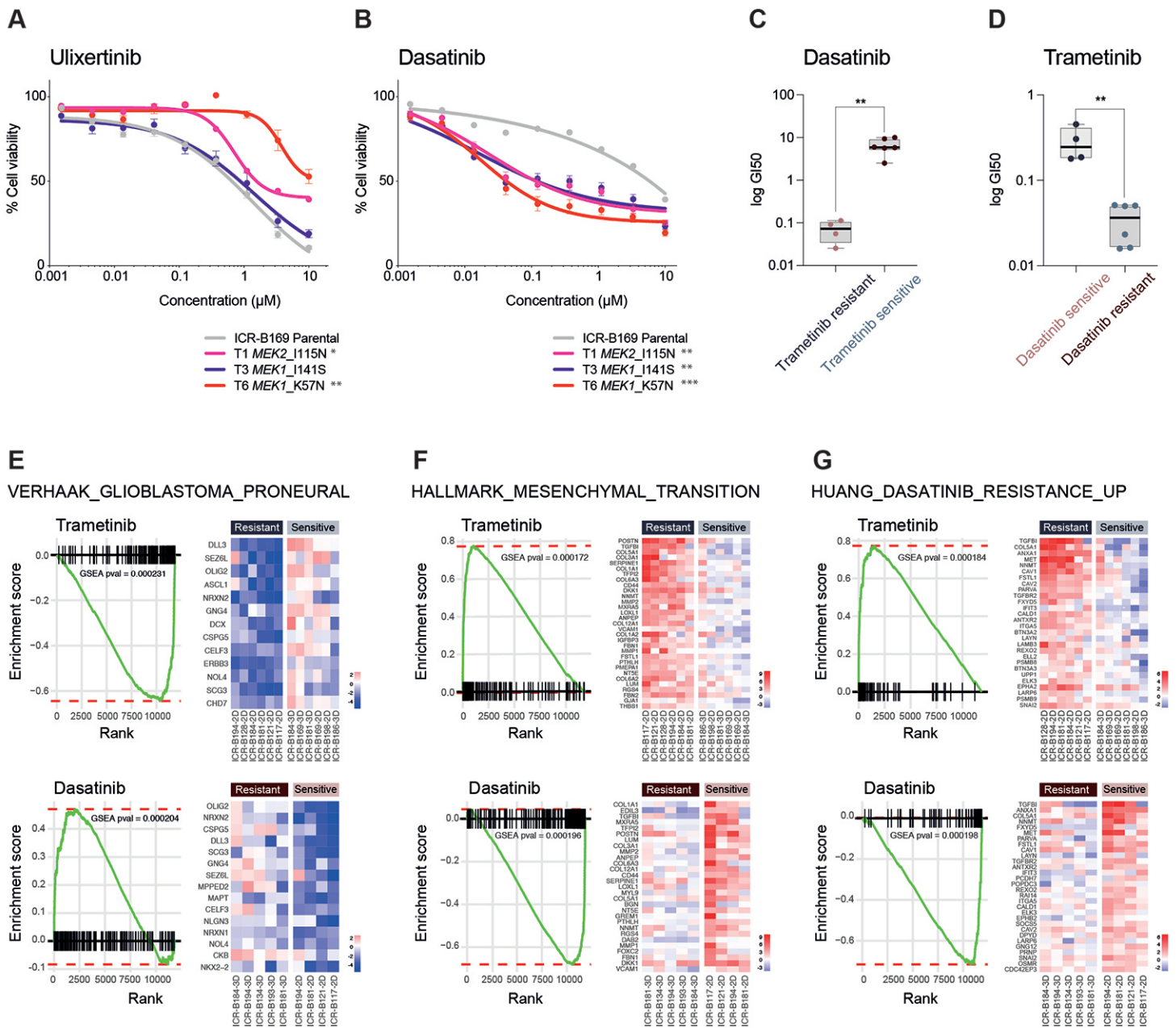
A

PIK3R1
NM_181523

N564D

SH3   RhoGAP   SH2   SH2_PIK3R1   SH2

B

NF1
NM_000267

I1824S

RasGAP   PH_NF1

C

Trametinib - ICR-B181

— 2D wild-type
— 3D *PIK3R1*_N564D ****

% Cell viability

Concentration (µM)

D

Trametinib - ICR-B184

— 2D wild-type
— 3D *NF1*_I1824S ****

% Cell viability

Concentration (µM)

E

ERK1/2$^{T202/Y204}$

phospho/total ERK1/2

2D 3D   2D 3D
ICR-B181   ICR-B184

F

ICR-B181 - *PIK3R1* N564D

*PIK3R1*_N564D AF

···· ICR-B181-3D
···· ICR-B181-2D

p5   p13   p15   p17/18
Passage number

G

ICR-B181-CDX

Percent survival

— ICR-B181-2D
— ICR-B181-3D

0   100   200   300   400
Time (days)

H

ICR-B181-CDX from 3D

Human Nuclear Antigen (HNA)

I

Sagittal T2-weighted MRI

J

Haematoxylin and eosin

Figure 3

Sagittal T1-weighted post-gadolinium MRI

Figure 4

Figure 5

Figure 6

Figure 7

A

B

AACR American Association
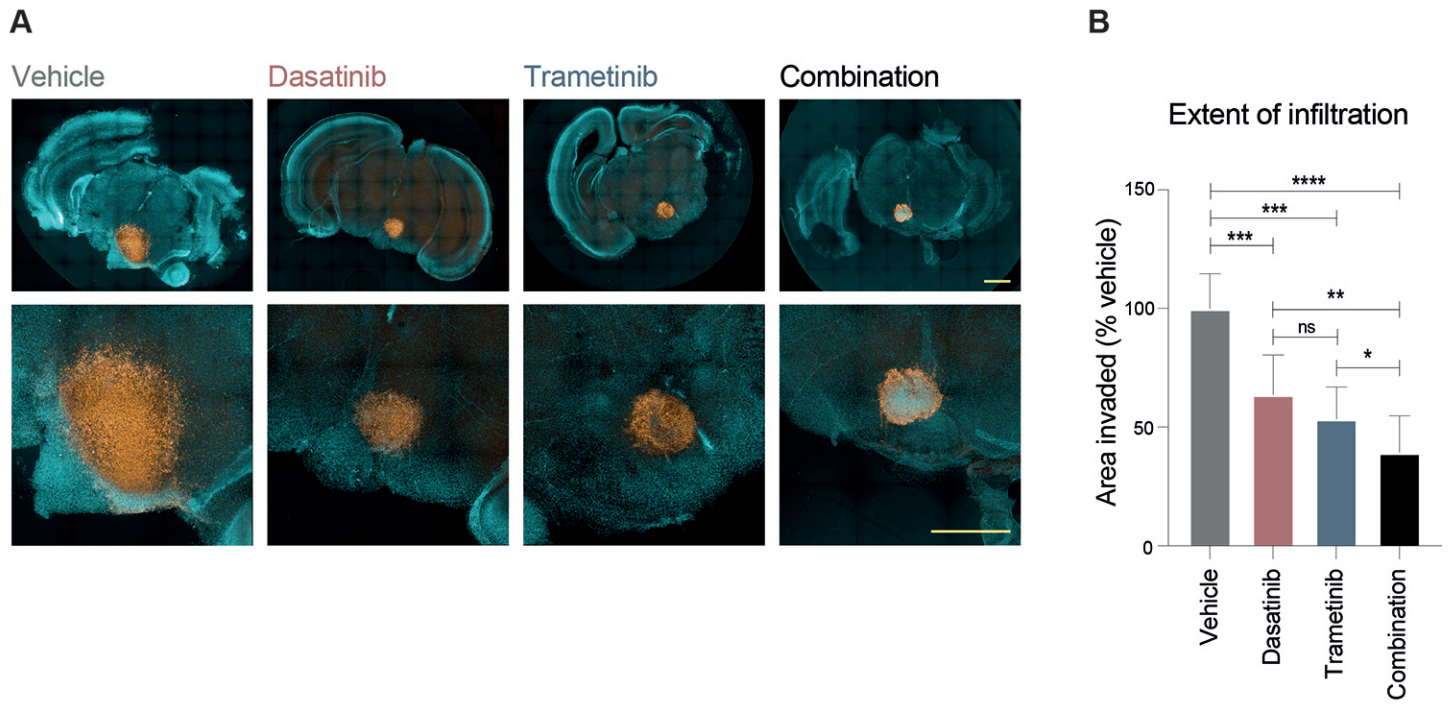for Cancer Research
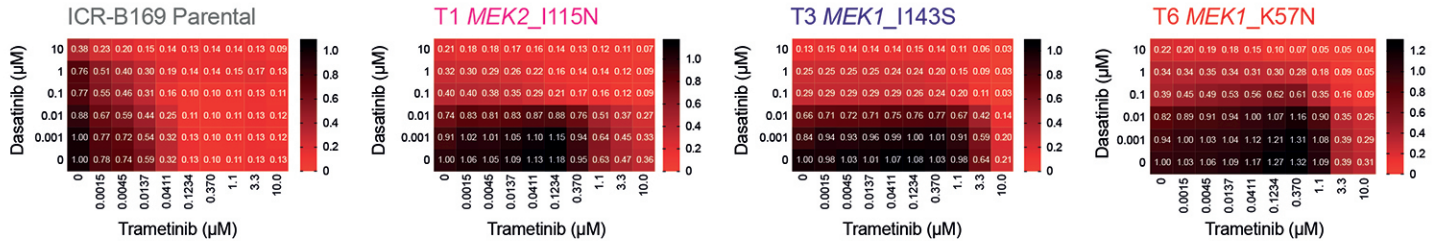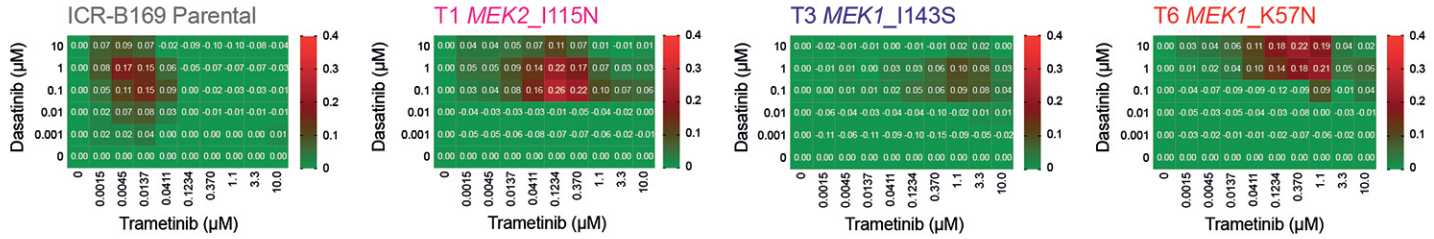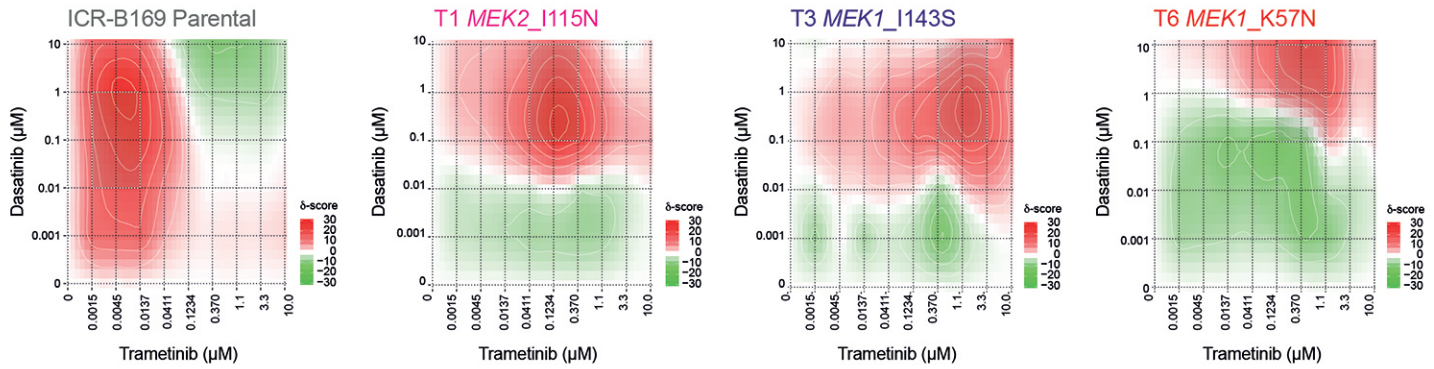
CANCER DISCOVERY

DIPG harbour alterations targetable by MEK inhibitors, with acquired resistance mechanisms overcome by combinatorial inhibition

Elisa Izquierdo, Diana M Carvalho, Alan Mackay, et al.

Cancer Discov Published OnlineFirst November 4, 2021.

Updated version	Access the most recent version of this article at: doi:10.1158/2159-8290.CD-20-0930
Supplementary Material	Access the most recent supplemental material at: http://cancerdiscovery.aacrjournals.org/content/suppl/2021/11/02/2159-8290.CD-20-0930.DC1
Author Manuscript	Author manuscripts have been peer reviewed and accepted for publication but have not yet been edited.

E-mail alerts	Sign up to receive free email-alerts related to this article or journal.
Reprints and Subscriptions	To order reprints of this article or to subscribe to the journal, contact the AACR Publications Department at pubs@aacr.org.
Permissions	To request permission to re-use all or part of this article, use this link http://cancerdiscovery.aacrjournals.org/content/early/2021/11/01/2159-8290.CD-20-0930. Click on "Request Permissions" which will take you to the Copyright Clearance Center's (CCC) Rightslink site.